Ultrasound Tomography

Nicole V. Ruiter, Michael Zapf, Torsten Hopp, Hartmut Gemmeke

Abstract Ultrasound tomography (USCT) is a promising imaging modality, mainly aiming at early diagnosis of breast cancer. It provides three-dimensional, reproducible images of higher quality than conventional ultrasound methods and additionally offers quantitative information on tissue properties. This chapter provides an introduction to the background and history of USCT, followed by an overview of image reconstruction algorithms and system design. It concludes with a discussion of current and future applications as well as limitations and their potential solutions.

1 Introduction

Ultrasound Tomography (USCT) is an exciting technology with several active research groups investigating new algorithms, devices, and applications around the globe. The basic idea of USCT is to surround the object to be imaged as much as possible with many ultrasound transducers and collect unfocused ultrasound data from many different angles. An exemplary setup is shown in Fig. 1.

The main application of the method is imaging of the female breast for early cancer detection. In the following sections, most examples will be given from breast cancer diagnosis. However, other applications are also possible and will be presented in later sections.

The potential benefits of USCT have been known for a long time. First publications in this field date back to the 1970s, e.g. Schomberg [1]. The main advantages of USCT systems are simultaneous recording of two or three dimensional images of reflection, attenuation and speed of sound, high image quality, and fast data acquisition of a large volume.

The construction of such a device for clinical practice was not successful for a long time - mainly because of the huge data rate and the time-consuming image

Karlsruhe Institute of Technology, Postbox 3640, 76021 Karlsruhe, Germany e-mail: nicole.ruiter@kit.edu

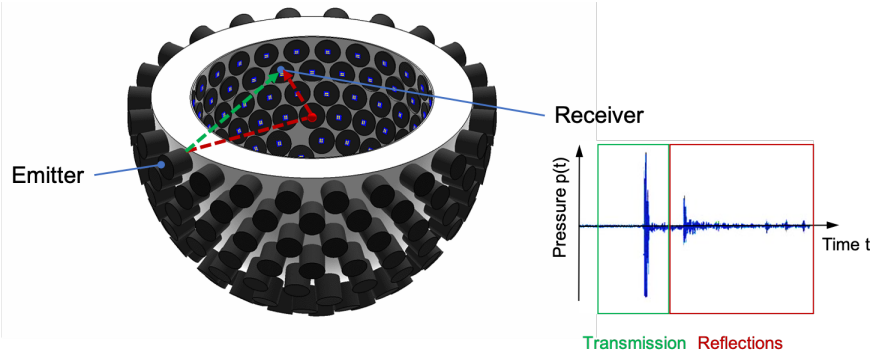

Fig. 1 Example of an USCT setup: A point scatterer (red sphere) in water is surrounded by ultrasound transducers (gray) in a fixed setup. One emitter emits a pulsed spherical wave. The pulse is scattered at the point scatterer. All transducers receive the resulting field. One exemplary A-scan is depicted on the right for the indicated emitter-receiver combination as pressure signal versus time. The first pulse corresponds to the pulse traveling on the fastest path from emitter to receiver (green, transmission), the second pulse is scattered at the point (red). More scattered and reflected pulses can occur, e.g. reflections on the water surface or other objects.

reconstruction. Currently, the first 2D and 2.5D systems have become available for clinical evaluation [2] [3] and the Delphinus system was FDA approved for screening in October 2021 [4].

Advantages of USCT

Ultrasound tomography offers the possibility to generate 3D volumes of the imaged object; deformation of soft tissue is not necessary due to non-contact imaging. Unlike X-ray procedures, the patient and operator are not exposed to radiation.

USCT produces multimodal images in one acquisition step, i.e. three different properties of the tissue can be reconstructed from one data set: Reflectivity, speed of sound, and attenuation. Reflectivity images show qualitative changes in acoustic impedance and thus represent interfaces between tissues in a manner similar to sonography.

Speed of sound and attenuation are quantitative values and can therefore be used to classify different tissue types [5]. For breast cancer diagnosis, initial experiments have shown that increased speed of sound values can separate cancer from normal tissue, e.g. [6]; in combination with attenuation this might be a good classifier for breast cancer [7, 8]. This type of quantitative information is only acquired with the USCT method and not with conventional sonography. Fig. 2 shows an example for the KIT 3D USCT system of a fused reflectivity image overlayed with thresholded speed of sound image indicating a large cancer in comparison with the MRI contrast enhancement of the same patient.

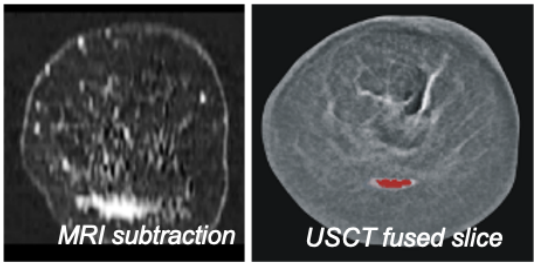

Fig. 2 Example of an USCT fused information: On the left side, the MRI subtraction image indicates the position of the cancer. The right image shows a reflectivity slice approximately at the same position with overlayed region of high speed of sound for this patient.

Due to the defined patient positioning without deformation of the soft tissues, the volume images of the patients are reproducible and operator-independent. This is a major advantage for follow-up examinations: Older images can easily be compared with new ones in order to detect small tissue changes for cancer diagnosis at an early stage.

The USCT device itself, device maintenance and the imaging are very cost-effective. The costs for breast imaging can be comparable to mammography and are therefore significantly lower than, for example, magnetic resonance imaging (MRI). The image acquisition can be carried out by a medical-technical assistant without the presence of a doctor. This enables the method to be used very widely, e.g. also by resident doctors.

Challenges of USCT

The challenges of building and operating an ultrasound tomography device are due to the large volume of a complex object being imaged, e.g. the female breast, compared to the wavelength of the ultrasound. Additionally a large number of unfocused ultrasound transducers is required to image the object, which need to be as identical as possible.

In order to approximate spherical waves (3D systems) or cylindrical (2D systems), the individual transducers have to be very small, resulting in low sound level pressures and a low signal-to-noise ratio.

The large number of ultrasound transducers that have to be recorded in parallel leads to a large number of parallel channels required and a high data rate in order to avoid patient motions with the shortest possible data acquisition times.

Due to the complex interaction of ultrasound with tissue, reconstruction algorithms for high image quality are complex [9]. A compromise has to be found between clinically relevant computing time and resulting image quality. Suitable three-dimensional reconstruction algorithms and parallel computing have to be investigated and further developed.

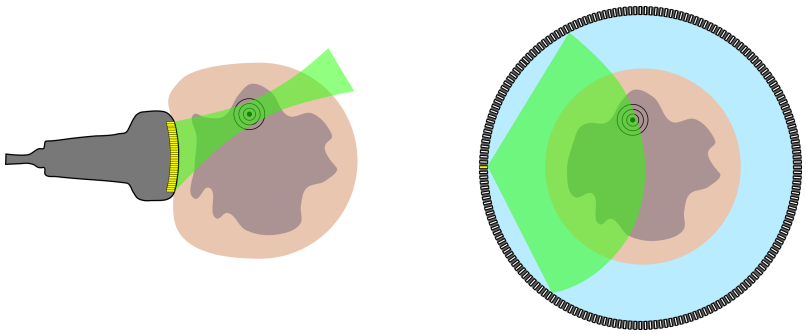

Fig. 3 Sonography (left) and USCT (right) acquisition modes. For sonography, a phased array focuses on one point in the imaged object. The focused beam is steered to acquire a slice image. For USCT, unfocused waves are emitted by each transducer sequentially. The acquired signals are then focused during the reconstruction.

The overall design of the devices should be robustly applicable in clinical practice, low-cost and designed to have a low power consumption.

Definition of USCT and Differences to Sonography

In order to differentiate USCT as precisely as possible from conventional ultrasound applications in medicine, a few key aspects need to be pointed out. Ultrasound tomography is a diagnostic procedure with its main application in the diagnosis of breast cancer. Contrary to conventional sonography, the object to be imaged is surrounded in a fixed setup by ultrasound transducers and sonicated in such a way that both reflection and transmission images of the speed of sound and attenuation distribution can be reconstructed.

Reflectivity tomography, as applied in conventional sonography, does generate a qualitative representation of the gradient of the body's acoustic impedance. However, the resolution of the resulting B-scans in sonography is anisotropic and spatially highly variable. This can be overcome with USCT by optimizing the transducer distribution and using unfocussed emission and reception. A diagram of the different acquisition modes is given in Fig. 3.

The relatively high speckle noise of sonography can, on the one hand, provide indirect information about the tissue as a diagnostic tool, and on the other hand, can obstruct important features. Speckle is the typical grainy background pattern in sonography images and is caused by interference effects [10]. Speckle can be reduced by spatial compounding. Compounding means that B-scans from different acquisition angles are added together. USCT systems include compounding due to their surrounding aperture, i.e. the object is imaged from many sides with ultrasound transducers.

3D ultrasound systems allow imaging of a 3D volume. However, the 3D volume at an imaging position corresponds to only a small part of the imaged object. If the entire volume has to be represented, many volumes must be recorded over the entire body region of interest. These partial volumes are then subsequently assembled. A recent development in breast ultrasound is, for example, Automated Whole-Breast Ultrasound (AWBU, SonoCine) [11], which images reflectivity volumes of the entire breast. This procedure results in more objective images and structured documentation than is common with ultrasound examinations. However, the systems only image from one side with conventional US scanners, resulting in anisotropic and spatially variable resolution and decreasing signal-to-noise ratio with penetration depth.

2 State of the Art of Ultrasound Tomography

The first use of ultrasound in medical diagnostics was published in 1942 by the psychiatrist and neurologist K. Dussik of the University Hospital of Vienna as "hyperfonography" [13]. The transmission-only system recorded so-called "ventriculograms", i.e. attenuation projections of ultrasound pulses through the human skull. The application was intended to examine the ventricles in the brain. For this purpose, the back of the patient's head was placed in a water bath and transilluminated by two opposing single transducers. A photograph of the apparatus can be found e.g. in [12]. However, the strong attenuation and reflection of ultrasound from the skull bone meant that this method was not pursued.

Howry, Holmes, and colleagues [14, 15] developed several prototypes, so-called compound scanners, which used a single focused transducer to compose B-scans from A-scan lines. USCT-like features were the placement of the patient in a water bath and the ability to move the transducer in a circular path around the patient. The "sonoscope" of 1954 is e.g. reprinted in [12].

From the mid-1950s onwards, further research was almost entirely limited to pulse-echo systems. Transmission devices or surrounding systems no longer played a role [12]. In the late 1970s and early 1980s, the idea of tomography for reflection slice images was revisited and analyzed theoretically and with computer simulations by Norton and Linzer, among others. In particular, they discussed how the aperture type affects the point spread function (PSF) of the resulting images. Different aperture types were considered, from spherical [16] to planar and cylindrical [17] to circular apertures [18].

At the same time, the idea of transmission imaging in the form of transmission tomography was revived by several groups for various applications [1, 19–23]. Greenleaf and Bahn published clinical results on transmission tomography of the breast [5], in which they showed a diagram, still often cited today, see Fig. 11, of the relationships between speed of sound and attenuation of normal and abnormal tissues of the breast. Further experiments were performed on Doppler and reflectivity tomography [24].

Combined systems that provided both transmission and reflection data from the breast were described by Müller et al. in 1979 [25] and by Carson and colleagues in 1981 [26]. Carson et al. used two directional, opposing ultrasound transducers with 3.5 MHz center frequency and 40% bandwidth. These were rotated and lifted around the patient's breast in the prone position to produce slice images in the frontal plane of the breast.

Current Systems

Most current USCT systems acquire both reflectivity and transmission data and focus on breast cancer diagnosis. Basically, systems can be divided into three types according to their aperture: 2D ring apertures, 2.5D segment, or 3D apertures. They operate at frequencies from 0.35 to 8 MHz and transmit unfocused ultrasound pulses in 2D or 3D. Acquisition times of the more sophisticated systems are in the range of minutes. The total time is dominated by the duration of the movements of the apertures; the travel times of the pulses are almost negligible with current systems.

Image reconstruction is computed offline in minutes to hours, often using massive parallelization in clinical trials, e.g. [27–31]. Since most groups do not provide detailed information on the acquisition time, only an approximate overview can be given. From the available system parameters, it is estimated that recordings with patients take between two and ten minutes per breast. Clinical trials have been described for systems from QT Imaging, Inc. (formerly QT Ultrasound and TechniScan) [3, 32], Delphinus Medical Systems [2, 33], MastoScopia [34], and KIT [35]. Delphinus stands out for reporting by far the largest number of patients.

The used reconstruction algorithms for transmission images are iterative algorithms, whereby the Algebraic Reconstruction Technique (ART) [36] is mostly preferred. This reconstruction method assumes straight rays in the simplest case or, in extended implementations, can also represent refraction effects [37]. Neglecting diffraction leads to a limited resolution of transmission volumes, see Section 4. This is where QT Ultrasound and Delphinus stand out. The system of QT uses a transmission reconstruction based on the paraxial approximation [38], which offers much higher resolution than ART. Delphinus even uses 2D full-waveform inversion tomography [39]. However, these approaches have the disadvantage that the required computation time is increased massively. Most systems use the Synthetic Aperture Focusing Technique (SAFT) [40] or spatial compounding for reflectivity imaging. Reconstructions are performed on multiple parallel GPUs for clinical use, e.g. [28, 29].

For 2D systems the resolution is anisotropic in the image plane and in the slice direction. It is depending on the bandwidth of the used pulses, the used aperture shape and is location dependent [41]. The 2D approaches result in images with slice thicknesses in the millimeter range. In addition, the images show limited depth of field. Focusing the transducers in the slice direction results in loss of out-of-plane reflections. Due to the required motion mechanics, the acquisition time cannot be

Table 1 Overview of a selection of current USCT systems

System	Modality	Aperture	Freq. range (Bandwidth)	No. elements	Motion	In vivo or clinical test
ANAÏS [42]	Transmission Reflection	Semicircle	3.0 MHz (75%)	1024	Rotation Translation	no
QT Scanner 2000 [43]	Transmission Reflection	Planar arrays Circular segments	0.9 MHz (100%) 3.6 MHz (70%)	8x256 3x192	Rotation Translation	[3, 32]
MUT [44, 45]	Transmission	Planar Arrays	8 MHz (50%)	128	Rotation Translation	[34]
SoftVue [28, 31]	Transmission Reflection	Ring	2.75 MHz (100%)	2048	Translation	[2, 33]
Prototype us CT [46]	Transmission Reflection	Ring	3 MHz (unk.)	2048	Translation	[46]
BUTIS [47]	Transmission Reflection	Ring	2.25 MHz (unk.)	1024	Translation	[47]
3D USCT II [48]	Transmission Reflection	Semi-ellipsoid	2.5 MHz (60%)	2041	Rotation Translation	[35]

reduced to sound-only time. A full 3D aperture using spherical wave fronts for imaging solves these limitations.

An overview of current USCT systems and their properties are listed in Table 1.

3 Ultrasound Propagation in Tissue

Imaging procedures are based on the interaction of energy with matter. Most medical procedures introduce energy into the body and record its interaction with the imaged structures. A certain imaging procedure thereby maps one or more defined physical properties of the tissues. This mapping can be qualitative or quantitative. For accurate medical diagnosis, the mapping of physical properties for normal and abnormal tissues have to be as well known and distinguishable as possible [49].

Ultrasound propagation in soft tissue is characterized by complex interaction. According to [50], these diverse interactions between ultrasound and tissue are the

greatest advantage of ultrasound-based diagnosis and, at the same time, its greatest weakness: They enable many applications and modalities of diagnostic ultrasound from Doppler to elastography to pulse-echo sonography. However, individual effects are difficult to isolate. Therefore, quantitative imaging is often not possible.

Acoustic Wave Equation and Assumptions

Ultrasound describes the phenomenon of propagation of density and pressure fluctuations in an elastic medium at frequencies greater than 20 kHz. Typical assumptions for the description of wave propagation in soft tissue are [10, 51]:

1. the medium "soft body tissue" behaves like a liquid. Thus, ultrasound waves propagate approximately only as longitudinal waves, i.e. compressional waves. Shear waves can be ignored.
2. the propagation is described by a linear wave equation as the amplitudes of the sound pressure and the particle displacement are very small.
3. the energy loss in the propagation of the sound wave is so small that absorption can be modeled in a simplified way. Dispersion effects can be neglected.
4. the medium is approximately isotropic, so that the material properties in homogeneous tissue can be described by a direction-independent scalar.

With the above assumptions, ultrasound propagation in soft tissue can be described by the acoustic wave equation [51]:

$$\nabla^2 p(\mathbf{x}) + k_0^2 \eta(\mathbf{x})^2 p(\mathbf{x}) - \frac{1}{\rho(\mathbf{x})} \nabla \rho(\mathbf{x}) \nabla p(\mathbf{x}) = 0 \tag{1}$$

where $p(\mathbf{x})$ is the spatially dependent pressure, $\rho(\mathbf{x})$ is the spatially dependent density, and $\eta(\mathbf{x})$ is the spatially dependent refractive index; k_0 is the wave number of the background medium.

If lossless propagation is assumed, the refractive index can be calculated as

$$\eta(\mathbf{x}) = \frac{c_0}{c(\mathbf{x})} = \sqrt{\frac{K_0}{\rho_0}} \sqrt{\frac{\rho(\mathbf{x})}{K(\mathbf{x})}} \tag{2}$$

where c_0 is the speed of sound of the background medium, $c(\mathbf{x})$ is the spatially dependent speed of sound, ρ_0 is the density of the background without sound propagation, and K_0 and $K(\mathbf{x})$ are the compression moduli of the background and medium, respectively.

If absorption is assumed to be small over the distance of a wavelength, the refractive index can be written as

$$\eta(\mathbf{x}) \approx \frac{c_0}{c(\mathbf{x})} + i \frac{\mu(\mathbf{x})}{k_0} \tag{3}$$

with μ as the spatial and frequency-dependent absorption coefficients. Attenuation α is often calculated instead of the absorption. This describes the total of the energy loss due to absorption and scattering [52]. The attenuation is thus partly also dependent on the aperture, since scattered energy components play a role, which are not detected by the finite active area of the aperture [50].

With these assumptions, sound propagation in inhomogeneous media depends on three parameters [53]: the density ρ, the adiabatic compression modulus K, and the absorption μ. Mostly these or derived properties such as the speed of sound $c = \sqrt{\frac{K}{\rho}}$, the attenuation α, and the gradient of acoustic impedance, $Z = \rho c$, as "reflectivity" I, are reconstructed during image generation.

Wave equations that model tissue not as a fluid but as an elastic solid, and thus include shear waves, can be found e.g. in [51].

4 Image Reconstruction

The image reconstruction reconstructs the object properties from the measured values such as ultrasound amplitude and phase. In general, if the relationship can be described relatively simply, the reconstruction can be performed quickly and effectively. When the relationship is complex, as in the case of ultrasound propagation in tissue, either limitations in the quality of reconstructed images have to be accepted or more sophisticated reconstruction algorithms have to be used, provided that current technology can compute them in finite time. For a given imaging system, the "quality", i.e. the resolution, the contrast and the correspondence with the true values of the reconstructed images, mainly depends on the reconstruction method used. The reconstructed values can be either quantitative or qualitative.

The reconstruction methods of USCT are based on the acoustic wave equation for inhomogeneous media with the assumptions described in section 3. The resulting main effects for the propagation of a wave are often modeled in a simplified manner as diffraction, refraction, scattering and absorption. Table 2 summarizes the approximations of the reconstruction methods described below and their properties.

Wave-based reconstruction methods, distinguished here as Full-Waveform, Paraxial, and Diffraction Tomography, can be grouped into two categories [54]: Full-Waveform Tomography which uses (almost) all information of the received waves and Paraxial and Diffraction Tomography, which use approximations for the reconstruction.

Full-Waveform Tomography

Full-waveform inversion (FWI) or waveform tomography [55] uses a forward model that approximates the measured data based on an initial estimate of the object properties to be reconstructed. A new model of the object properties is generated

Table 2 Overview of USCT reconstruction methods using approximations based on [37]. λ is the wavelength, L is the distance between emitter and receiver, p is the ultrasound pressure, y a direction normal to the main propagation direction, p_s is the scattered pressure, ∂p the change of pressure, k the wave number and c_0 the speed of sound.

Method	Approximation	Resolution	Complexity	Assumption
Paraxial	Anisotropic field	$\lambda/2$	High	$\partial^2 p/\partial y^2$ small
Born	Linearization of pressure	$\lambda/2$	High	$p_s \ll p$
Rytov	Linearization of phase	$\lambda/2$	High	$\delta p \ll 1$
Eikonal	Infinite frequency	$\sqrt{L\lambda}$	Middle	k small
Ray propagation	Infinite frequency	$\sqrt{L\lambda}$	Low	c_0 const.

from the difference between the measured and simulated data. These steps are iterated using a suitable optimization algorithm until a termination criterion is reached, i.e. the difference of the object model and the measured data is small. The advantage of this method is that the wave equation does not need to be linearized and therefore all effects of wave propagation, within the stated assumptions in section 3, are modeled. The object itself is discretized, which allows, for example, the solution of the wave equation using finite elements [55]. A disadvantage is that this method requires the highest computational effort.

First implementations for ultrasound tomography have been published in recent years, e.g. [56–58]. However, these methods are currently limited to low frequencies below 0.5 MHz or 2D reconstructions [39,57,59]. Most of these approaches assume that the density in the tissue is constant and only the compressibility varies. Results with simulated data for simultaneous reconstruction of density and compressibility can be found in [60,61].

In detail the published methods vary greatly, especially in the underlying formulation of wave equation, e.g. with or without absorption, and whether the forward model is calculated in the time or in the frequency domain. The following brief introduction to the theory and the reconstruction methods closely follows [57] by applying Contrast Source Inversion in the frequency domain. For simplicity, the introduction is done without modeling absorption and the density is assumed to be constant, i.e., only the spatially varying speed of sound $c(\mathbf{x})$ is considered. The theory and reconstruction for this particular method, including absorption and density reconstruction, can be found in [54].

The Helmholtz equation for heterogeneous media in the frequency domain is

$$\nabla^2 \hat{p}(\mathbf{x}) + \frac{\omega^2}{c^2(\mathbf{x})} \hat{p}(\mathbf{x}) = -\hat{S}(\mathbf{x}), \tag{4}$$

where $\hat{p}(\mathbf{x})$ is the pressure field at location $\mathbf{x}$ in the frequency domain. $\hat{S}(\mathbf{x})$ is the primary source generating the sound field. ω is the angular frequency and ∇^2 the Laplace operator.

The total pressure field is seperated into the incident field $\hat{p}^{inc}(\mathbf{x})$ and the scattered field $\hat{p}^{sct}(\mathbf{x})$ as

$$\hat{p}(\mathbf{x}) = \hat{p}^{inc}(\mathbf{x}) + \hat{p}^{sct}(\mathbf{x}). \tag{5}$$

The incident field is the part of the pressure field generated by the source $\hat{S}$ which is traveling through homogeneuos background medium with c_0 and the scattered field is a correction term which accounts for the deviations due to the imaged object with $c(\mathbf{x}) = c_0 + \triangle c(\mathbf{x})$.

The scattered field can be written as

$$\hat{p}^{sct}(\mathbf{x}) = \omega^2 \int_{\mathbf{x}' \in \mathbb{D}} \hat{G}(\mathbf{x} - \mathbf{x}')\hat{p}(\mathbf{x}')\chi(\mathbf{x}')dV(\mathbf{x}'), \tag{6}$$

where $\mathbb{D}$ is the spatial domain, i.e., the reconstructed area or volume (V), $\hat{G}$ is the Green's function, and the contrast function $\chi(\mathbf{x}')$ is the deviation from the background medium caused by the object, with

$$\chi(\mathbf{x}') = \frac{1}{c^2(\mathbf{x}')} - \frac{1}{c_0^2}. \tag{7}$$

For Contrast Source Inversion in two dimensions, i.e. $\mathbf{x} = (x, y)^T$, the total field in equation (5) and the scattered field in equation (6) are modified such, that the contrast function $\chi(\mathbf{x}')$ and the total field are combined in one variable $\hat{w}(\mathbf{x}') = \hat{p}(\mathbf{x}')\chi(\mathbf{x}')$, i.e.

$$\hat{p}(\mathbf{x}) = \hat{p}^{inc}(\mathbf{x}) + \omega^2 \int_{\mathbf{x}' \in \mathbb{D}} \hat{G}(\mathbf{x} - \mathbf{x}')\hat{w}(\mathbf{x}')dA(\mathbf{x}'), \tag{8}$$

with $\mathbf{x} \in \mathbb{S}$ and

$$\hat{p}^{sct}(\mathbf{x}) = \omega^2 \int_{\mathbf{x}' \in \mathbb{D}} \hat{G}(\mathbf{x} - \mathbf{x}')\hat{w}(\mathbf{x}')dA(\mathbf{x}'), \tag{9}$$

with $\mathbf{x} \in \mathbb{S}$ and $\mathbb{S}$ the surface of the domain $\mathbb{D}$.

After discretization and in operator notation, the equation (8) is written as

$$\hat{\mathbf{p}}_j = \hat{\mathbf{p}}_j^{inc} + \mathbf{L}^{\mathbb{D}}[\hat{\mathbf{w}}_j], \tag{10}$$

where $\hat{\mathbf{p}}_j$ is the discretized total field, $\hat{\mathbf{p}}_j^{inc}$ the discretized incident field, $\mathbf{L}^{\mathbb{D}}$ the integral operator on $\mathbb{D}$, and $j = 1, 2, \ldots, J$ denote the unique emitter and receiver combinations.

if the equation (10) is multiplied by $\boldsymbol{\chi}$ and solved for the incident field, the resulting equation is called object equation

$$\boldsymbol{\chi}\hat{\mathbf{p}}_j^{inc} = \hat{\mathbf{w}}_j - \chi\mathbf{L}^{\mathbb{D}}[\hat{\mathbf{w}}_j], \tag{11}$$

where $\hat{w}_j$ are the contrast sources.

Equation (9) can be rewritten in a similar way and expressed as the so-called data equation

$$\hat{\mathbf{f}}_j = \mathbf{L}^{\mathbb{S}}[\hat{\mathbf{w}}_j], \tag{12}$$

where $\hat{\mathbf{f}}_j$ is the measured data, i.e., a set of measurements of the scattered field at $\mathbb{S}$, and $\mathbf{L}^{\mathbb{S}}$ is the integral operator over $\mathbb{S}$.

The aim is to reconstruct the contrast function χ for given $\hat{\mathbf{f}}_j$. This is done iteratively by minimizing the error for the object equation (11) and the error for the data equation (12), which is a measure of how well a current estimate of $\hat{\mathbf{w}}_{j,n}$ predicts $\chi\hat{\mathbf{p}}_j^{inc}$ and $\hat{\mathbf{f}}_j$, respectively. The initial values of the contrast source $\hat{\mathbf{w}}_{j,0}$, the total field $\hat{\mathbf{p}}_{j,0}$ and the contrast function χ_0 are calculated directly from the data equation (12) using the measured values. In the following iteration, first the contrast source $\hat{\mathbf{w}}_{j,n}$ is updated based on the current error. Then, the total field $\hat{\mathbf{p}}_{j,n}$ is caculated for the updated contrast source. Finally, the contrast function χ_n is calculated by direct minimization from $\hat{\mathbf{w}}_{j,n}$ and $\hat{\mathbf{p}}_{j,n}$. This is repeated until a threshold for the total error or a certain number of iterations is reached.

Finally, the speed of sound values of the domain are calculated from the resulting χ as

$$\mathbf{c} = \frac{1}{\sqrt{\chi + c_0^{-2}}}. \tag{13}$$

Diffraction Tomography

The term diffraction tomography is also used in the literature for full-wave(form) methods. Here, the classification according to [9] is used, which distinguishes diffraction tomography from FWI tomography by applying additional simplifying approximations.

Typical reconstruction methods are based on the Born or the Rytov approximation in the first order of the wave equation [62]. Diffraction tomography has so far been used mainly on simulated 2D data sets with low frequencies, e.g. [24, 63–65]. The Born approximation assumes that objects to be reconstructed are small and their acoustic parameters are only weakly distinguishable from the background. The Rytov approximation constrains the maximum contrast of objects. Both assume non-absorbing media, so absorption or attenuation has to be modeled additionally. The advantage of diffraction tomography is that the reconstructions can be up to a hundred times faster than the FWI methods [66]. However, the assumptions are of limited use for imaging breast tissue [9, 57] and other tissues with highly varying speed of sound. Extensions of the Born approximation such as the Distorted Wave Born Approximation can improve this, e.g. [67], but are again more complex to compute.

The following short introduction focuses on the Born approximation in two dimensions as descibed in [57]. The Born approximation simplifies the scattered field in equation (6) to

$$\hat{p}^{sct}(\mathbf{x}) = \omega^2 \int_{\mathbf{x}' \in \mathbb{D}} \hat{G}(\mathbf{x} - \mathbf{x}')\hat{p}^{inc}(\mathbf{x}')\chi(\mathbf{x}')dA(\mathbf{x}'), \tag{14}$$

where the total field $\hat{p}(\mathbf{x}')$ is approximated by the incident field $\hat{p}^{inc}(\mathbf{x}')$.

Discretized and in operator notation, the scattered field can be rewritten as

$$\hat{\mathbf{p}}_j^{sct} = \mathbf{M}[\chi], \tag{15}$$

where $\mathbf{M}$ is the integral operator.

The aim of the reconstruction is again to calculate χ from the measured data, denoted here as $\hat{\mathbf{p}}_j^{sct}$.

Simple Backpropagation reconstructs χ directly from the scattered field

$$\chi = \mathbf{M}^\dagger[\hat{\mathbf{p}}_j^{sct}], \tag{16}$$

where $\mathbf{M}^\dagger[\hat{\mathbf{p}}_j^{sct}] = \sum_{j,\omega} \omega^2 [\hat{\mathbf{p}}_j^{inc}(\mathbf{x'})\hat{G}(\mathbf{x}^r - \mathbf{x'})]^* \hat{\mathbf{p}}_j^{sct}(\mathbf{x}^r)$ is the adjoint of the integral operator $\mathbf{M}$ and * denoting the complex conjugate.

In the so-called Born inversion χ is calculated iterativley, e.g. by minimizing $E_n = ||\hat{\mathbf{p}}_j^{sct} - \mathbf{M}[\chi_n]||$. This corresponds to finding a contrast function that best fits the measured data. Before the first iteration step, χ_0 is set to 0. Then χ_n is calculated based on the previous difference E_{n-1} between measured data and contrast function. This is repeated until E_n is smaller than a threshold or a certain number of iterations is reached.

In both cases, the speed of sound distribution of the reconstructed image can be calculated using χ_n in equation (13).

Paraxial Tomography

Reconstructions based on the paraxial approximation are often used in geophysics [68]. In paraxial tomography, the wave propagation is computed mainly in one direction and the contributions from other directions are neglected. This reduces the required computational power since the wave propagation can be computed by an iterative layer-by-layer wave transport. Refraction, diffraction and forward scattering are taken into account. Absorption can be modeled additionally. This reconstruction method has already been successfully applied to clinical data for speed of sound and attenuation reconstructions of a 2.5D system [3] that emits approximately plane waves. It has been extended for the use with spherical waves [69] recently, which will allow broader application to the more common USCT setups with cylindrical and spherical waves in future. A quite effective method is to learn the forward model and to reconstruct the paraxial tomography with a neural network [70].

The brief introduction in the theory follows [69]. For simplicity, the density is considered constant, the problem to be two-dimensional, and the medium lossless. Note that for the paraxial approximation, the 2D problem is ususally denoted by x and z, where z is the direction in which the plane wave travels, i.e., the paraxial direction.

The inhomogeneous Helmholtz equation (4) may then be rewritten as

$$\nabla^2 \hat{p}(\mathbf{x}) + k_0^2 (1 + \eta(\mathbf{x}))^2 \hat{p}(\mathbf{x}) = 0, \tag{17}$$

where $k_0 = \frac{\omega}{c_0}$ is the wave number of the background and η is the refractive index.

The paraxial approximation of the Helmholtz equation is found by first transforming the pressure $\hat{p}$ with $\hat{p} = e^{ik_0 z}\hat{u}$ to an equation of its envelope with

$$\partial_{xx}\hat{u} + \partial_{zz}\hat{u} + 2ik_0\partial_z\hat{u} + k_0^2((1+\eta(\mathbf{x}))^2 - 1)\hat{u} = 0. \tag{18}$$

The envelope $\hat{u}$ contains the deviation of $\hat{p}$ from a plane wave. Introducing operator $Q = \sqrt{1 + (\frac{1}{k_0^2}\partial_{xx} + (1+\eta)^2 - 1)}$ and assuming that η varies only very slowly in z direction ($\partial_{zz} \approx 0$), the equation (18) can be factorized into two parts

$$(\partial_z + ik_0 + ik_0 Q)(\partial_z + ik_0 - ik_0 Q)\hat{u} = 0, \tag{19}$$

The first part on the left hand side describes the propagation of the wave in $-z$, i.e. the reflected wave, and the right part in $+z$ direction, i.e. the transmitted wave.

Considering only the wave propagation in $+z$ direction, the paraxial approximation can be written as

$$\partial_z\hat{u} + ik_0(1-Q)\hat{u} = 0. \tag{20}$$

The forward problem, i.e., the calculation of $\hat{p}$ for given η and $\hat{p}^{inc}$ can now be solved numerically by the split step formulation. The pressure $\hat{\mathbf{p}}_{n+1}$ at position z_{n+1} is calculated based on $\hat{\mathbf{p}}_n$ at z_n, $n = 1...N$,

$$\hat{\mathbf{p}}_{n+1} = e^{ik_0\eta_n\triangle z}\mathcal{F}^{-1}\{e^{ik_0\sqrt{1-(\frac{2\pi}{\triangle x N k_0})^2}\triangle z}\mathcal{F}\{\hat{\mathbf{p}}_n\}\}, \tag{21}$$

with $\mathcal{F}$ the (discrete) Fourier transformation over space. Setting $\hat{\mathbf{p}}_0 = \hat{\mathbf{p}}^{inc}$, one can incrementally calculate the pressure at discrete z_n.

Different approaches have been proposed for the backward problem of reconstructing c from known $\hat{\mathbf{p}}^{inc}$ and measured data $\hat{\mathbf{f}}$. In [69], the problem is solved similarly to the Born inversion described in the previous subsection by iteratively minimizing the error between the measured data and the simulated data for the current estimate of η with $E_n = ||\hat{\mathbf{p}}_j^{sct} - \mathbf{p}_N||$. For this simple case, it is assumed that the receivers are located at z_N.

Ray Tomography

In ray tomography, an ultrasound pulse is assumed to travel on an infinitely thin beam. Diffraction and scattering are thus neglected. This assumption is based on the limiting case for infinitely small wavelengths or infinitely high frequencies, similar to the assumptions for geometrical optics. Allowing for refraction of the ray, the Eikonal ray approximation is obtained. For rays traveling directly from emitter to receiver without refraction, the straight ray approximation is obtained, see Fig. 4. Both approaches are used for transmission tomography, i.e. either the speed of sound or the attenuation distribution can be calculated using the pulses received on the fastest or shortest paths from emitter to receiver, respectively.

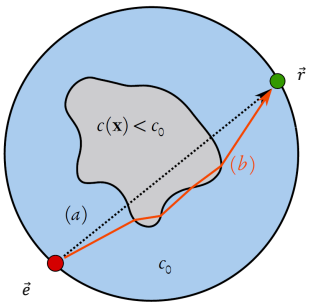

Fig. 4 Example for straight and refracted beams from [37]: Path (a) is the shortest and path (b) the fastest path connecting emitter **e** (red) and receiver **r** (green).

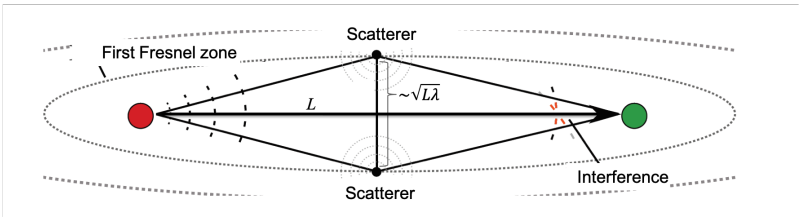

Fig. 5 First Fresnel zone of emitter (red) and receiver (green): L is the distance of emitter and receiver. Adapted from [37].

In Eikonal tomography, the refracted path between transmitter and receiver is calculated iteratively on a current voxel model of the object. The model of the object is then recomputed for these new paths. Examples of Eikonal tomography for 2D systems are [1, 71, 72] and for 3D systems [73].

Straight ray tomography is based on the most limiting approximation, neither refraction, diffraction nor scattering are considered. However, since it is very fast to compute, it is widely used, e.g. [20, 21, 37, 74].

In contrast to previous methods, the achievable resolution of the resulting images is very limited in ray tomography techniques. Because diffraction and scattering are neglected, effects from the first Fresnel zone around the direct path are ignored [75]. The first Fresnel zone corresponds in 2D to an ellipse with emitter and receiver at the focal points and includes all scatterers that can interfere with transmission, see Fig. 5. The position of scatterers located in this zone cannot be unambiguously determined without modeling diffraction and scattering. This leads to uncertainty in the position reconstruction, which in the worst case corresponds to the maximum width of the first Fresnel zone of $\sqrt{L\lambda}$, where L is the distance from emitter to receiver and λ is the wavelength of the wave [76]. Thus, for 2.5 MHz in water, an L of 20 cm results in a position uncertainty of about 1 cm.

One method for reconstructing sound speed images [77] is to discretize the problem and write the forward problem as

$$\mathbf{As} = \mathbf{b}. \tag{22}$$

Here, the matrix $\mathbf{A}$ describes the paths the rays travel through the slowness map $\mathbf{s}$ to generate the arrival time measurements in $\mathbf{b}$. The slowness map is the inverse of the speed of sound map, i.e. $s_j = 1/c_j$.

Since $\mathbf{A}$ is usually very large and sparse and the problem is often ill-posed, direct inversion is often not possible. Hence the speed of sound distribution of the imaged object is then iteratively calculated by minimizing an error term describing the differences between the simulated and measured arrival times, e.g., $E = ||\mathbf{As} - \mathbf{b}||^2$.

Reflection tomography

Reflection tomography [17] also assumes straight rays between the emitter, reflector and receiver. However, the reflected amplitude of the ultrasound is used to reconstruct images. Reflection tomography is based on the Born approximation. In the simplest case, this assumes constant speed of sound, negligible attenuation, and single scattering. Reflection tomography is related to the B-scan method of conventional sonography. There, however, the optimal focus is only achieved at the focal point of the beam during transmission, whereas with USCT reflection tomography an ideal focus can be generated at any point in the image. This is due to acquiring fully unfocused data which is then focused to each point during the reconstruction. Many USCT systems use the Synthetic Aperture Focusing Technique (SAFT) [40] for reconstruction of reflectivity images.

The reconstruction can be performed in one step, e.g., in [57] described as

$$\chi = \sum_{j,\mathbf{t}} \mathbf{p}_j^{sct}(\mathbf{t})\delta(c_0\mathbf{t} - ||\mathbf{x}^s - \mathbf{x}|| - ||\mathbf{x}^r - \mathbf{x}||), \tag{23}$$

with j all combinations of emitters $\mathbf{x}^s$ and receivers $\mathbf{x}^r$ and $\mathbf{t}$ the discrete time samples of the measured field $\mathbf{p}_j^{sct}$.

Clinical Applicability of Reconstruction Methods

So far USCT devices with their algorithms are aimed at high image quality and are used for image-based diagnosis. In contrast to sonography, it is not mandatory to acquire and reconstruct the images in real-time, because comparable to MRI, a structured volume is generated that can be stored and analyzed without the patient. The main challenge is to acquire the raw data fast enough to prevent blurring due to patient motion and enabling clinical applicability by reconstructions in the range of minutes to hours.

Since there is a certain amount of time available for reconstruction, the best possible image quality should be the main goal in the selection of possible algorithms. However, reconstructions based on the wave equation are very computationally expensive. Currently, only a few algorithms are available that have been tested with real data, and only two examples are used with clinically relevant timing with parallel hardware [38, 39]. They trade off by using frequencies well below 1 MHz, limiting the possible resolution.

The reconstruction methods, with the exception of simple ray and reflection tomography, generally use time-consuming iterative methods to solve the inverse problem. The two simpler methods can, in principle, be computed directly without iteratively estimating the object to be imaged. An exception is the algebraic reconstruction method (ART) for ray-based transmission tomography, where the iterative solution is used to solve an ill-posed inverse problem. Fig. 6 shows a simplified comparison of the computational complexity of the algorithms as a function of the number of pixels or voxels in one direction (N) and the non-parallelized time duration. Not included in this overview is the potential of the algorithms for parallelization or use of alternative reconstruction methods. Some examples can be found in [66, 70, 78].

The O-notation [79] is used to classify the complexity of the algorithms. It describes how the runtime and memory requirements change as a function of the size of the input parameters. The following assumptions were made for the input parameters:

- Number of discrete image points: in 3D $N = n_x = n_y = n_z$ with n_x, n_y, n_z the number of points in each direction. An overall number of N^3 voxels have to be

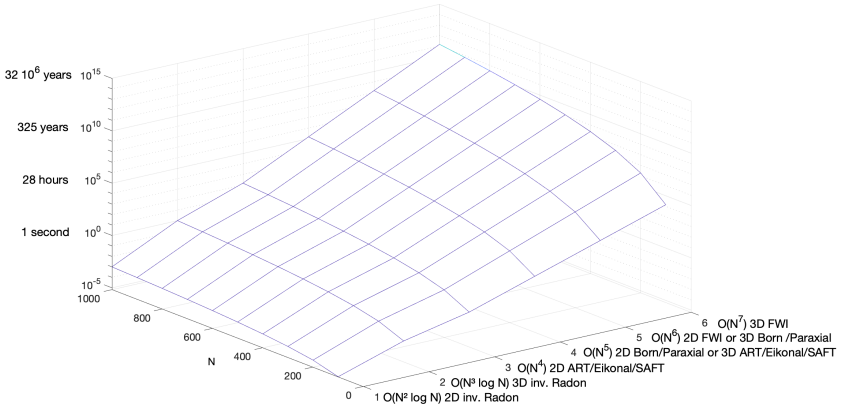

Fig. 6 Simplified comparison of the complexity of reconstruction algorithms used for USCT based on the assumption that 3D Fourier transform could be calculated in 1 s for N = 1000.

reconstructed. In 2D $N = n_x = n_y$ and $N_s = n_z$ number of slices in z direction and $N_s \ll N$. An overall number of $N_s \cdot N^2$ pixels have to be reconstructed.
- Number of emitters and receivers: $N = N_e = N_r$ with N_e number of emitting positions and N_r number of receiving positions per emission. The number is each assumed to be equal to N, which fits roughly the Nyquist theorem in 2D and results in N^2 A-scans.
- Number of iterations for iterative algorithms: N_{iter}, with $N_{iter} \ll N$
- Number of swept frequencies for algorithms which use discrete frequencies: N_f, with $N_f \ll N$
- Number of time samples in each A-Scan: N_t, with $N_t = N$

Given these assumptions simple ray and reflection tomography algorithms are in the range of $O(N^2 logN)$ to $O(N^5)$ which equals e.g. to a calculation in the range of seconds to minutes for 2D systems. On the other end, full-waveform tomography has a complexity of $O(N^6)$ in the 2D and $O(N^7)$ in the 3D case resulting in computation times in the range of days to months and years depending on the image resolution.

The system design strongly influences the computational complexity and limits the applicability of certain methods. For example a fully unfocused 3D system [35] offers better 3D point spread function and less artifacts, but the third dimension increases the computational requirements for reconstruction by a significant factor. In comparison, for a 2D system [28] only 20 slices per breast need to be computed, but for a 3D system more than 1000 slices are generated. Thus, additional accelerations and approximations are necessary for reconstruction in a clinically applicable time frame [66].

Resources for USCT Data

A direct comparison of different implementations of algorithms is difficult, since they are usually applied to custom simulated data or - if available - real data. The relatively few experimental data sets are usually not widely available. Also, the different experimental setups usually require many adjustments for data processing and system modeling for the reconstruction algorithms. To address this gap, a USCT data exchange and collaboration initiative was launched to provide open and easy-to-use data and code interfaces and to stimulate the exchange of available reconstruction algorithms and raw data sets from different USCT instruments.

The reference database [80] was established with freely available and openly licensed USCT data. It provides a tool for direct comparison of algorithms using the same data for reconstruction. Simulated data as well as real-world data sets are available. Fig. 7 shows the real-world datasets. The first three phantoms were imaged using KIT's 3D USCT, the fourth using TU Delft's DBUS with a 2D low-frequency setup, and the last using the 2D system MUBI from the Spanish National Research Council and Complutense University Madrid [81]. In addition, feedback on data and system architecture from scientists working on the reconstruction will help drive further development of measurement setups.

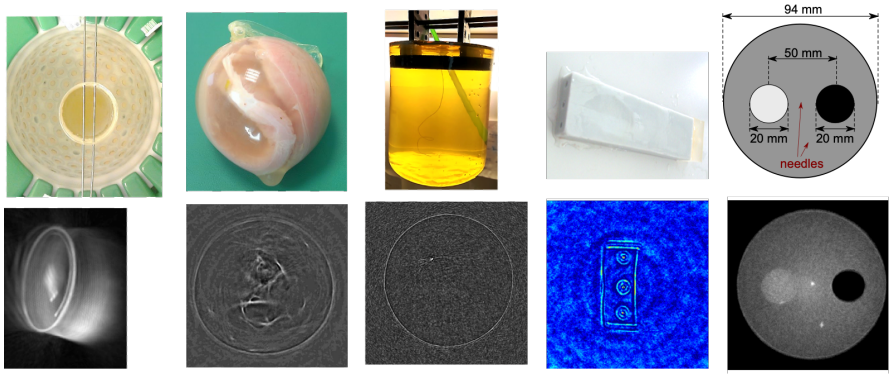

Fig. 7 Real world phantoms of the USCT exchange platform (from left to right): gelatin, turkey, thread, agar and tissue mimicking phantom with each SAFT reconstructions or spatial compounding (bottom right).

5 Technical Challenges and System Design

A USCT device should both generate data that enables optimal imaging results and be suitable for clinical use, including patient safety and comfort, high patient throughput, and low cost of acquisition and operation. The practical challenges in developing such a system are summarized below.

Transducer Distribution

The 3D distribution of ultrasound waves in the measured volume has to be sampled temporally and spatially to obtain digitized data for the reconstruction. Similar to the sampling theorem for temporal signals, where the sampling rate and time window of an A-scan has to match the bandwidth and time duration used, the spatial sampling has to match the spatial frequencies of the imaged object, i.e., the inverse of the required resolution, and the object volume. The positions of the transducers during data acquisition define the spatial sampling points of the data. This is usually a compromise between optimal distribution and number of available transducers, either real available transducers or virtual positions, usually obtained by multiple movements of available transducers.

Ideally, for a 3D volume such as the female breast, spatial sampling points would completely surround the object and sample at distances of $\Delta x/2$, where Δx is the resolution of the resulting images. However, this is practically impossible due to the accessibility of the object to be imaged and constraints imposed by the cost and complexity of the device, the resulting data size, and the reconstruction time. Therefore, various approximations of such apertures, i.e., the set of physically available and virtual transducer positions, have been proposed so far. Fig. 8 shows diagrams and

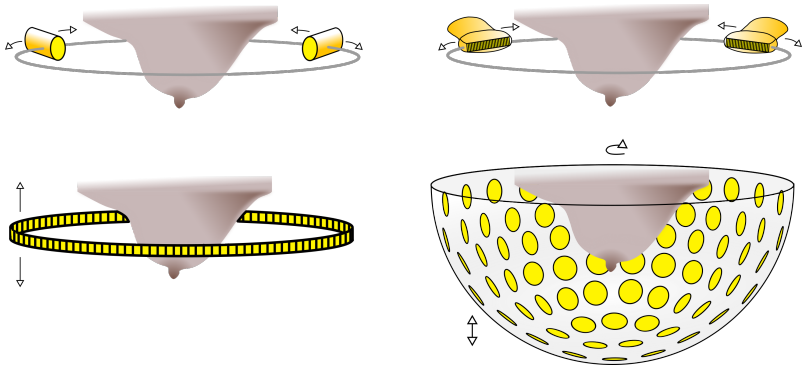

Fig. 8 Different setups for USCT systems imaging a breast are shown in this diagram. Top left: 2D slice acquisition with individual and freely positioned transducers (yellow). Top right: 2D slice acquisition with individual and freely positioned linear transducer arrays. Bottom left: 2D slice acquisition with a ring of transducers. Bottom right: 3D acquisition with hemispherical array. Arrows indicate the typical degrees of freedom for mechanical motion of the transducers.

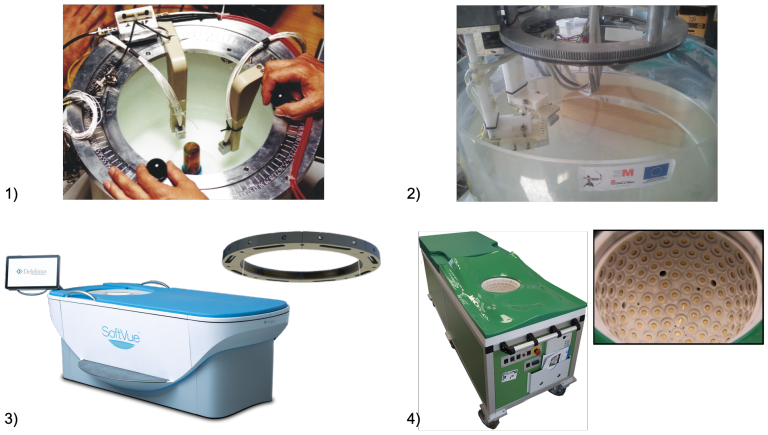

Fig. 9 Top left (1): 2D slice acquisition with individual and freely positionable transducers of the first experimental USCT at KIT [82]. Top right (2): 2D slice acquisition with individual and freely positionable linear transducer arrays of the first MUBI system [83]. Bottom left (3): 2D slice acquisition with a ring of transducers in Delphnius' SoftVue system (Courtesy of Neb Duric, CTO, Delphinus Medical Technologies). Bottom right (4): 3D acquisition with semiellipsoidal array of KIT's 3D USCT II [48].

Fig. 9 realizations of such setups. Virtual transducer positions are created by mechanically moving either individual transducers, sets of transducers, or all transducers to additional positions and repeating the measurements with these new positions. The disadvantage of this method is a longer data acquisition time and, if the transducers cannot be positioned individually, a limited pattern of overall positions.

Simple laboratory experiments use only a few individual transducers or conventional sonography scanners focused in azimuth direction. They are mechanically moved to many virtual positions and acquire the data from one 2D slice, e.g. [84]. Typical data acquisition times are many minutes to several hours. They are therefore mostly used for imaging phantoms.

For the use in paraxial tomography, systems with linearly grouped transducers have been used in 1D [85] and 2D arrays [86]. The transducers have to be rotated around the object and also moved in the azimuth direction to obtain virtual positions. It has been reported that data acquisition will take several minutes.

The most commonly used aperture design is grouping transducers on a ring, e.g. [31]. The ring is usually densely populated with transducers, e.g. 2048 transducers on a ring of 22 cm diameter for 3 MHz center frequency. The transducers are unfocused in x-y direction and focused in z (azimuth) direction. The ring is mechanically moved in z-direction and acquires data for 2D slices, with, for example, 20 to 40 slices. Typical duration for data acquisition is 1 to 5 minutes per breast. An interesting approach was proposed by [42]. There, the transducers were grouped on a semicircle with diameter 20 cm and the semicircle could be moved with two degrees of freedom, allowing also sagittal slices.

3D systems based on a cylinder, a half ellipsoid [48] and a hemisphere [87] have been presented. The number of transducers ranges up to 2304, so mechanical repositioning of the entire transducer aperture is also used to achieve denser sampling. The transducers transmit and receive approximately spherical waves for full 3D imaging. Data acquisition time ranges from 1 to 6 minutes. Due to the unfocused transducers, no reflections are lost between layers and isotropic resolution in 3D is possible.

Ultrasound Transducers for USCT

The ultrasound transducers usually operate in the lower frequency range, i.e., 1 to 3 MHz, are required to have a large bandwidth and either emit or receive spherical waves for 3D imaging or cylindrical waves with azimuthal focus for 2D slice imaging. Typically, trade-offs are made between the resulting low local acoustic pressure and the need for an acceptable signal-to-noise ratio.

The frequency range and the 3D distribution of the generated ultrasound field is mainly dependent on the geometry of the active elements of the transducers. The thickness of the element in direction of the deformation sets the resonance frequency, the shape and the diameters the angular characteristic, see Fig. 10 for examples.

The frequency range of most systems is centered around 2 to 3 MHz, with a wide bandwidth, i.e. more than 50%. The center frequency is a compromise between image resolution and size of the imaged volume. The higher the frequencies, i.e., the smaller the wavelength λ, the higher the possible resolution, see Table 2. However, ultrasound absorption also increases with frequency. The local sound pressure is additionally reduced by the propagation of the wave as a function of the distance traveled. Thus, the use of high frequencies is limited by the size and absorption of the

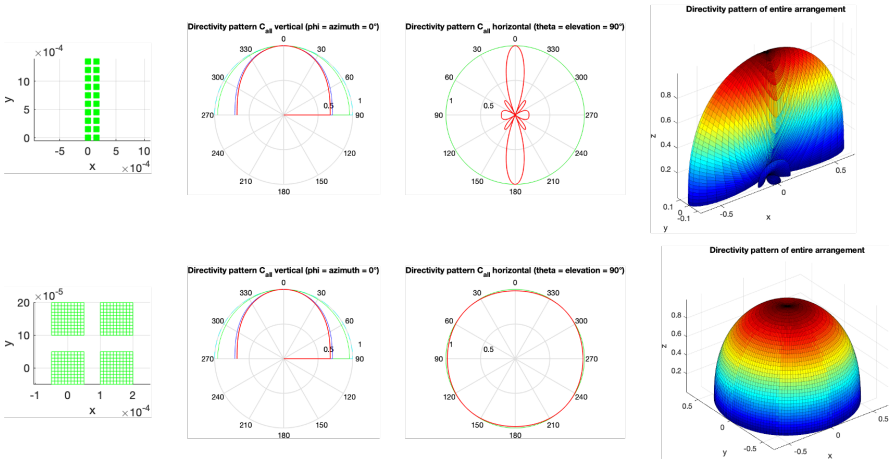

Fig. 10 Beam patterns of a rectangular and a quadratic transducer element: Top: Rectangular element with 0.25 mm x 1.45 mm area. Bottom: Quadratic element with 0.25 mm x 0.25 mm area. Both for a 2.5 MHz excitation in water. Left: Active area in m. Left center: -3 dB intensity limit in xy-plane (red). Right center: -3 dB intensity limit in yz-plane (red). Right: -3 dB surface in 3D. Both elements emit in z-direction.

object and the total distance of the transducers in the aperture, since the sensitivity of the receivers is limited. Currently, systems operating at lower frequencies around 1 MHz are becoming more popular [39, 88]. This is because FWI and paraxial tomography have become computationally feasible at these lower frequencies. They also have additional advantages, e.g., they can be applied to body parts that contain bone, such as joints or the skull, due to the lower absorption, and also reduce the overall complexity of the system by allowing for less dense spatial sampling.

A 2D system would typically use a rod-shaped active element, see Fig. 10 top row, with large opening angle in xy direction and narrow angle in azimuth direction to image approximately 2D slices. The thickness of the slice can be further reduced with acoustic lenses. Note that the layer thickness is smaller near the transmitter and increases with distance. Thus, the total layer thickness is an average value. A 3D system usually uses square or disk-shaped transducers, see Fig. 10 bottom row, to achieve large opening angles in 3D.

Since the transducers in most systems have small active areas and are fired individually, the amplitude of the emitted pressure and the sensitivity of the receivers is low, resulting in a low signal-to-noise ratio. For this reason, the area of the active element is often set as a compromise between ultrasound pressure and opening angle. Also, amplification electronics may be present near the transducers and the gain of the channels can be set individually or object-specific and time-dependent. Some systems additionally use a so-called coded excitation [89]. The advantage of coded excitation is that the emitted ultrasound energy can be distributed over time and

recovered in the form of a much shorter decoded pulse, which significantly increases the SNR.

Data Acquisition and Processing

For a short duration of imaging and especially to avoid blurring of data due to patient movement, data acquisition in systems for medical use must be fast and is performed with hundreds of parallel channels. Computing power for reconstruction has to be high to obtain images in clinically relevant time.

Data acquisition and image reconstruction are often performed separately in USCT devices: After the fastest possible data acquisition, the data are stored in the device or on an external storage medium for offline image processing.

After data acquisition, the signals are preprocessed and image reconstruction is performed. The separation into two systems has several advantages: The development of the data acquisition hardware can be decoupled from the development of the reconstruction algorithms and their platform. Heat generation and appropriate countermeasures in the device need only be considered for the data acquisition (DAQ) hardware. The reconstruction algorithms and corresponding acceleration hardware can be adapted to some extent during the clinical trial, since changes to the device itself are often only possible with renewed approval. For more complex reconstruction algorithms with longer computation times, the device can be used to continuously image patients without waiting for the reconstruction to finish. One drawback is the additional time required to transfer data from the USCT device to the reconstruction hardware, which can be significant due to the large amount of raw data acquired.

Calibration

Calibration is an important part of initialization and maintenance of USCT systems. It can be divided into spatial calibration, temperature calibration and calibration of the measurement chain of signals.

Spatial calibration involves determining the position of the transducers. For high resolution imaging, the position must be known better than $\lambda/2$, e.g., for 2.5 MHz this would correspond to an accuracy better than 0.3 mm. This could be achieved by building the aperture and transducers with high precision. Alternatively, the positions can be determined by measurements, see e.g. [42, 90].

Since ultrasound travels through water over long distances and the speed of sound in water depends on temperature, this must also be monitored. Here, calibration of the internal temperature measurement devices may be necessary, or temperature or speed of sound can be calculated from empty measurements using known transducer positions.

The measurement chain of the signal contains the individual system responses of the transducers and the measurement channels. The transducers can differ in center frequency, bandwidth, sensitivity, and aperture angle. The DAQ channels can

introduce delays and also have frequency-dependent transfer functions. Options for calibration of these channels are: 3D hydrophone measurements of the transducers, short-time measurements of the transfer functions of the channels, and the use of empty measurements. More detailed information can be found, for example, in [91].

Medical Products and Standards

Finally, the device must comply with the standards for medical devices in order to be applicable to the patient. These include the use of biocompatible materials, hygiene concepts for the water bath and other surfaces, ultrasound safety with limitation of the applied ultrasound energy and maximum pressure values, electrical and mechanical safety and electromagnetic compatibility (EMC). For the clinical use of the method, extensive clinical studies have to be performed to demonstrate the advantages and limitations of the method.

6 Applications and Current Limitations of USCT

The USCT method opens up exciting new possibilities for ultrasound imaging, providing high-quality images comparable to MRI with the added benefit of being quantitative. USCT is being developed primarily as a tool for imaging in breast cancer prognosis, with other applications, e.g. joint and brain imaging, currently being explored. Other potential applications include combination with other modalities, e.g., photoacoustics, Doppler, etc., and use in therapy.

Nevertheless, the method is currently limited by the fundamentally different transducer setup compared to conventional sonography and the relatively long duration of data acquisition and image reconstruction, especially when compared to the real-time imaging capabilities of sonography.

USCT and the Breast

Breast cancer is one of the most common cancers in women in the Western world [92]. Approximately one in ten women will develop breast cancer during their lifetime. Because early and mid-stage breast cancer is usually asymptomatic, screening is offered in many countries. The central goal of breast cancer screening is to detect tumors as early as possible and to avoid false positive diagnoses. Currently, the main method is X-ray mammography with sonography or MRI as a secondary diagnostic procedure. The USCT method is a promising candidate to improve the sensitivity and specificity of the current method, as it can also image the attenuation and speed of sound.

A number of early studies were performed to distinguish breast and cancer tissues based on their attenuation coefficients and speed of sound values [7, 93–96].

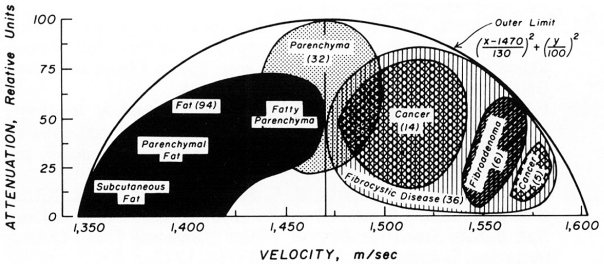

Fig. 11 Diagram of attenuation over speed of sound for normal and suspicious tissues of the female breast from Greenleaf and colleagues, reproduced from [5]. Speed of sound is shown on the x-axis and normalized attenuation on the y-axis.

Greenleaf and Bahn [5] published a correlation between attenuation and speed of sound with a USCT system in 1981, see Fig. 11. Here, different tissue types can be roughly classified by their combined values for attenuation and speed of sound. Similar results have been found with more recent USCT scanners, e.g. [97–99].

Based on these results, several research groups are currently working on USCT systems for breast cancer diagnosis. In some cases, companies have been formed that are developing commercial systems and have FDA approval. Smaller clinical trials have been conducted by several groups and larger clinical trials have been started to show how effective the method is.

Delphinus Medical Technologies was founded in 2010 as a spin-off from the Barbara Ann Karmanos Cancer Institute [28]. They reported successful smaller studies [2] and also engaged tracking the progress of chemotherapy [100] and breast density estimation for risk classification [101]. Their large clinical study [102] with approx. 8500 asymptomatic patients was completed in July 2021 and the system was FDA approved for screening in October 2021 [4]. An very impressive comparison between MRI and speed of sound images of different patients is given in Fig. 12.

QT Imaging, Inc. (formerly Techniscan and QT Ultrasound) reported successful clinical studies, the most recent publication being comparing speed of sound images with mammograms [32]. They have also conducted a smaller study on estimating breast density for risk classification [103]. They completed a large study with approx. 750 patients in March 2021 [104].

The 3D USCT II of KIT was evaluated in a smaller pilot study [35] and is currently employed in a concordance study. The successor system is aimed at a larger multi-center study to be started in 2022 [87].

For the MUT system of Mastoscopia good results in distinguishing benign and malignant smaller lesions (< 15 mm) with 71 patients [34] was reported.

Other upcoming systems are planning or have started trials, e.g. [46, 47].

Although USCT is not yet a standard of clinical practice, clinical trial results and FDA approval of the first device for breast cancer screening demonstrate the method's potential for the future.

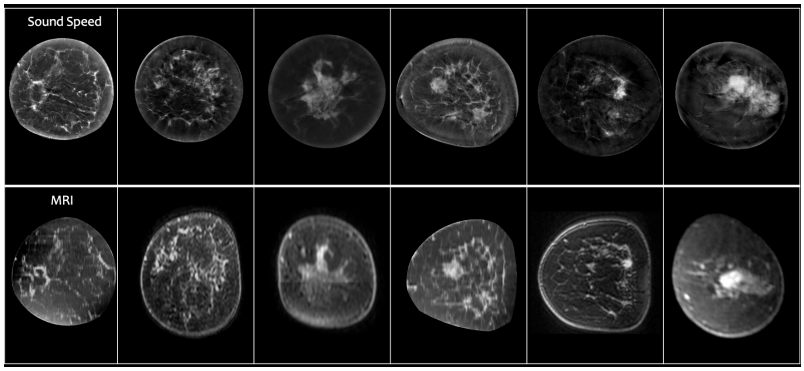

Fig. 12 Comparison of coronal speed of sound and MRI slices of different patients for the Delphinus Softvue system. Speed of sound in the top row and MRI in the bottom row. Courtesy of Neb Duric, CTO, Delphinus Medical Technologies.

Beyond the Breast: More Applications of USCT

The female breast has been the main application of USCT systems because it is relatively easy to access from many angles and does not contain bone or other ultrasonically hard structures. Bone is highly attenuating to ultrasound at high frequencies, and because of its high density, the assumptions in section 3 are not tenable. Nevertheless, the following experimental applications of USCT systems show that imaging is possible with some adjustments. This pioneering work could open the application to many other parts of the body.

Joints

First, Lasaygues and colleagues [105] published several papers on USCT of ex vivo bones and obtained impressive results. Ding [47] and colleagues demonstrated initial slice images of the arm and leg of a living subject.

Wiskin and colleagues examined imaging of a cadaveric knee [106, 107]. They used fused images from reflectivity and paraxial tomography and compared them to MRI. They were able to reproduce the 3D geometry of the knee in great detail and the sound velocity values of the soft tissues (fat, muscle, tendon, cartilage) agreed very well with values from the literature. They extended this work in a study of limited angle tomography [108]. The applications of these images could be in the diagnosis, monitoring, and grading of muscular dystrophy and osteoarthritis.

Brain Imaging

Guasch and colleagues [109] investigated 3D FWI tomography of the brain in simulations and real experiments. They simulated a hemispherical 3D array of 1024 low-frequency transducers in the range of 100 - 850 kHz. Brain structures including a simulated hemorrhage could be imaged with high resolution and high contrast. In addition, it was shown that ultrasound signals could be received with sufficient SNR through the skull of a subject at the low frequencies used.

Applications of this method could be in rapid diagnosis of stroke and head trauma as well as routine monitoring of various neurological diseases.

Ultrasound Therapy and USCT

Thermoablation is a therapeutic method in which focused ultrasound induces high temperatures above 60°C in a focal region, resulting in cell death within seconds [110]. The method is completely noninvasive and has the potential to replace conventional surgery of small tumors [111].

Conventional thermal ablation is currently at the stage of clinical trials and initial applications. Limiting factors are the long duration of up to several hours, difficult-to-control ultrasound focusing, local hot spots, and the need for image-guided monitoring [112].

USCT could directly monitor ablation using the change in speed of sound due to heating. It could also significantly speed up thermal ablation by applying multiple focal points similar to the method proposed by Fab [113]. The complex 2D phased array used there to generate the multiple foci could be replaced by a USCT system. In particular, 3D USCT with its many transducers positioned around the imaged object can be considered as a huge non-planar 2D array. With simultaneous application of all emitters and focusing on one point, the total acoustic pressure of all available transducers in such a system would result in foci with several megapascals of acoustic pressure, sufficient for thermal ablation [110]. Currently, the electronics of USCT systems are not designed to be triggered as a 2D phased array. Adapting the electronics is a task that is challenging but feasible.

Modalities Beyond Reflectivity, Speed of Sound and Attenuation

Conventional ultrasound systems can usually provide Doppler and sometimes elastography modes in addition to B-scan images. Doppler maps the local blood flow distribution and elastography images the tissue stiffness distribution. Both modalities provide valuable additional diagnostic information for cancer diagnosis and functional imaging. The modalities are feasible in principle with USCT systems. For Doppler, methods similar to those used by Jensen and colleagues [114] for SAFT-based Doppler imaging, i.e., synthetic aperture flow imaging, could be used. Currently, the major limitation is the DAQ speed of the USCT systems.

Spatial compounding for breast ARFI images was first developed and analyzed by Salido and colleagues [115]. A proposal and simulations how to perform elastography with a USCT system was given by Hopp [116]. There, strain elastography was realized using two USCT images of an undeformed and a mechanically deformed breast.

Microbubbles are tiny air bubbles used as contrast agents in conventional sonography [10]. The bubbles are injected into the patient and ultrasound is strongly reflected off the bubbles. They are used to image cavities, such as the heart or blood vessels, or to create nonlinear effects to increase image contrast. Alternatively, high sound pressure can be applied to destroy the bubbles. This is mostly used for therapy, e.g., local drug delivery or opening the blood-brain barrier.

Recent applications include rapid imaging of microbubbles and tracking their movements to produce super-resolution images of small vessels [117]. For this purpose, the so-called ultrafast ultrasound imaging methods [118] are used. There, plane waves from different angles are used to image the object with high repetition rates. Initial publications showed impressive results in imaging microvessels in a rat brain [119]. The use of ultrafast Doppler showed the possibility for functional imaging of the brain, which was previously only possible with MRI [118]. Similarly, Doppler imaging of microbubbles or super-resolution imaging can theoretically be applied in USCT systems, but is currently limited by the DAQ rate and, to some extent, the low acoustic pressures used in USCT.

Photoacoustics is a promising imaging technique based on laser-induced ultrasound. Short laser pulses cause locally the tissue to oscillate and are thus be a source of ultrasound waves. The emissions are recorded with ultrasound transducers in setups similar to USCT systems. The intensity of the emitted ultrasound depends on the absorbed light, i.e., the wavelength of the laser and the illuminated tissue type. In particular, red lasers can be used to produce impressive images of vascularization, i.e., the distribution of blood vessels, of structures such as cancerous tumors. However, the method is limited by the penetration depth of the light into the body. Therefore, and because of the similarity of the receiving aperture to USCT systems, combinations of the methods are currently being investigated, e.g. [120].

Beyond the already existing ultrasound modalities, additional information can be retrieved from the rich USCT data due to the complex interaction of the waves with the tissue, see Section 3. For example, the data can be used to generate scatter characteristics of pixels [121]. For reflectivity tomography, the reflected amplitudes of an image point are simply summed up. Thus, for directional scattering, the characteristic information of the scatterers is lost. SAFT can be extended to obtain reflectivity characteristics. Instead of summing over all A-scans, the two-dimensional reflectivity characteristics can be reconstructed for each voxel over angles. In the long term, this modality could also be used to obtain information similar to tissue-specific speckle texture in sonography.

Current Limitations and Possible Solutions

The current advantages of conventional sonography over USCT are the many applications, multiple established modalities, and real-time imaging.

The many applications, i.e., imaging of different body structures, are possible because sonography uses back reflection for imaging with linear arrays and the array are mainly in direct contact with the structure to be analyzed.

As a result, ultrasound travels smaller distances and body parts that are partially shadowed by bone or air-filled structures can be imaged without having to traverse these areas. However, as shown previously, it is possible to extend USCT imaging to areas that contain bone. Thus, this disadvantage of USCT may be overcome in the future at least partly, especially with the use of lower frequency ranges and advanced image reconstruction algorithms.

Enclosing the body with ultrasound transducers is challenging, and coupling to the patient by a water bath is also not very practical, see Fig. **??** (b). This could be solved, for example, with water-filled contact balloons or a flexible transducer aperture that can be placed directly on the patient surface. A hybrid approach could be to extend USCT image reconstruction methods to the use with limited angle view reconstructions, as shown by Wiskin [108].

In the future, the established modalities of sonography can either be implemented, improved, or extended with speed of sound and attenuation tomography. For future implementation of established modalities such as Doppler, the main challenges are the low acoustic pressure of USCT and the relatively slow data acquisition.

An established method of dealing with low sound pressure is the use of phased arrays to generate so-called virtual sources [122]. In contrast to focusing the sound beam as used in conventional sonography, the virtual sources are generated near the array and act as sources of approximately spherical waves. Since the entire active area of the phased array can be used to generate the virtual source, the total radiated sound pressure is approximately the same as in sonography. For this purpose, the transmitting electronics of the USCT systems have to be adapted to allow the individually delayed excitation of multiple transducers.

The current duration of data acquisition for USCT systems is limited primarily by the need to mechanically move the transducers. Other factors that increase the duration of data acquisition are multiplexing and the averaging factor of the systems. Multiplexing is used when more than one receiver shares a DAQ channel. Averaging involves acquiring the same A-scan from the same transmitter-receiver combination multiple times to add these A-scans together to increase SNR.

The lower limit for the duration of data acquisition is the time it takes for the ultrasound pulses to travel through the imaged volume. Since ultrasound is reflected and scattered in tissue, this is usually estimated by the longest distance from a transmitter to the furthest point plus the distance from that point to the furthest receiver. It depends on the spatial dimensions of the imaged volume or slice, the speed of sound range, and the transducer distribution. An additional waiting time is usually added to allow the sound intensity in the volume to decay to a certain

Table 3 Example duration of DAQ for different system specifications (rounded)

Row	**System**	d in cm	N_{em}	T_{prop} in ms	N_{mult}	N_{ava}	N_s	T_{mo} in s	T in s
1	2D ring	30	2,048	0.8	1	1	1	-	1.6
2		30	2,048	0.8	1	1	40	0.5	85.0
3		30	1,024	0.8	1	1	40	0.5	52.3
4		20	2,048	0.5	1	1	40	0.5	63.2
5		30	2,048	0.8	4	4	40	0.5	1068.1
6		22	1,024	1.0	2	1	20	1	59.0
7	3D hemisphere	30	2,048	0.8	1	1	1	-	1.6
8		30	2,048	0.8	1	1	4	0.5	8.1
9		30	2,048	0.8	4	1	4	0.5	106.4
10		22	4,579	0.6	1	1	1	-	2.7
11		24	628	0.6	3	8	10	30	360.4
12		36	2,304	0.8	6	4	2	20	108.5

threshold. This duration is then multiplied by the number of emissions for the device.

In sum the data acquisition time T of most systems can be calculated by:

$$T = N_s \cdot N_{em} \cdot T_{prop} \cdot N_{mult} \cdot N_{ava} + (N_s - 1) \cdot T_{mo}$$

with N_{em} the number of emissions, T_{prop} the propagation time of the ultrasound wave, N_{mult} the multiplex factor, N_{ava} the averaging factor, N_s the number of slices in a 2D ring system or the number of aperture positions in a 3D system, and T_{mo} the time for the mechanical motion. In Table 3 some examples are given. The first six rows give examples for a 2D system with a ring of transducers, the last six rows for a 3D system with a hemispherical aperture. The numbers given are based on current systems, and for each type of system the last rows estimate the values for existing systems, i.e. previous 2D ring of Delphinus [31] (row 6) and the two 3D systems of KIT [48, 87] (rows 11 and 12).

T_{prop} was simplified and calculated as $T_{prop} = 2 \cdot (2d)/c$ with d diameter of the ring, c speed of sound of water at 1500 m/s and doubling the time to fade the ultrasonic intensity.

In general, for all configurations, the data acquisition time is dominated by the time required to mechanically move the transducers, i.e. T_{mo} and especially for 2D systems by the averaging N_{ava} and the multiplex N_{mult} factors (row 5). Reducing the diameter d (rows 4) and the number of emitters N_{em} by a factor of 2 (row 3) does lead to a slight increased speed. As expected, the 3D system is faster compared to the 2D acquisition (e.g. rows 2 and 8), although it should be noted that the acquired amount of data is much sparser in most examples, i.e., for the 3D example (rows 8), only 10 % of the A-scans are acquired. For a hypothetical 3D system (row 10) with no motion and the same number of A-scans and diameter as the real 2D system (row 6), the DAQ time is less than 3 seconds compared to 1 minute.

The duration of data acquisition is limited only by the transit time of the ultrasound and the number of transmitting positions if the acquisition hardware and number of

transducers are optimized. However, for the given examples without motion (rows 1, 7, 10), the duration is still greater than 1 second. To approach higher frame rates, further developments are necessary, e.g. by simultaneous transmission at multiple positions with coded pulses as described by Misaridis [123].

The challenges of using the advanced image reconstruction algorithms are currently addressed by parallel computation (GPUs or FPGAs) using either simpler algorithms or 2D lower frequency systems. In the future, this could only be addressed by improved computational speed and more memory (Moore's law) or by advances in the reconstruction algorithms. A promising approach is to use neural networks for the advanced reconstruction algorithms, e.g. [70], since these require an enormous computational effort for training but, once trained, can perform reconstructions very quickly.

7 Summary

USCT is an old concept from the early days of medical ultrasound imaging, but only became technically feasible for clinical application in the last decade. Currently, several research groups around the globe are working on improving reconstruction algorithms, developing optimal setups, and are conducting clinical evaluation.

A major breakthrough in recent years has been the application of reconstruction methods that completely solve the acoustic wave equation, i.e., FWI and paraxial tomography. They now allow speed of sound imaging at high resolution and are beginning to rival MRI in contrast and diagnostic information. However, due to the large computational requirements, there are still many challenges to be solved before these methods can be widely used.

System design of an optimal device is still a subject of research. Due to the simplicity of the design, 2D ring systems are the most commonly built systems. However, they limit the overall measurement speed because many mechanical motion steps are required, and lead to large layer thickness and artifacts due to 2D data acquisition. Other setups will certainly become popular in the future, but the additional cost and complexity of the more sophisticated hardware has to be justified by significantly improved imaging results.

The clinical performance of the method is currently being evaluated for breast cancer diagnosis. The initial results are very promising. An extension to other application areas, e.g. imaging of joints or the human brain, seems possible but is still a field of early research.

References

1. H. Schomberg. An improved approach to reconstructive ultrasound tomography. *Journal of Physics D: Applied Physics*, 11(15):L181–5, 1978.

2. N. Duric, P. Littrup, C. Li, O. Roy, S. Schmidt, X. Cheng, J. Seamans, A. Wallen, and L. Bey-Knight. Breast imaging with SoftVue: initial clinical evaluation. In Johan G. Bosch and Marvin M. Doyley, editors, *Medical Imaging 2014: Ultrasonic Imaging and Tomography*, volume 9040, pages 208 – 215. International Society for Optics and Photonics, SPIE, 2014.
3. M. André, J. Wiskin, and D. Borup. *Clinical Results with Ultrasound Computed Tomography of the Breast*.
4. Inc. Delphinus Medical Technologies. Delphinus receives fda approval for its softvue 3d whole breast ultrasound tomography system. https://www.delphinusmt.com/news/delphinus-receives-fda-approval-for-its-softvue-3d-whole-breast-ultrasound-tomography-system/. Accessed: 2021-11-08.
5. J.F. Greenleaf and R.C. Bahn. Clinical imaging with transmissive ultrasonic computerized tomography. *IEEE Transactions on Bio-Medical Engineering*, 28(2):177–85, 1981.
6. T. Hopp. *Multimodal registration of X-Ray mammography with 3D volume datasets*. Ph.d. thesis, University Mannheim, 2012.
7. C. Calderon, D. Vilkomerson, R. Mezrich, K.F. Etzold, B. Kingsley, and M. Haskin. Differences in the attenuation of ultrasound by normal, benign, and malignant breast tissue. *Journal of Clinical Ultrasound*, 4:249–54, 1976.
8. S.A. Johnson, T. Abbott, R. Bell, M. Berggren, D. Borup, D. Robinson, J. Wiskin, S. Olsen, and B. Hanover. Non-invasive breast tissue characterization using ultrasound speed and attenuation. *Acoustical Imaging*, pages 147–54, 2007.
9. N. Duric, C. Li, O. Roy, and S. Schmidt. Acoustic tomography: Promise versus reality. In *IEEE International Ultrasonics Symposium, IUS*, pages 2033–41, 2011.
10. T.L. Szabo. *Diagnostic Ultrasound Imaging: Inside Out*. Academic Press, 2014.
11. K.M. Kelly and G.A. Richwald. Automated whole-breast ultrasound: Advancing the performance of breast cancer screening. *Seminars in ultrasound, CT, and MR*, 32(4):273–80, 2011.
12. J. Woo. A short history of the development of ultrasound in obstetrics and gynecology. http://www.ob-ultrasound.net/history1.html. Accessed: 2015-11-09.
13. K.T. Dussik. Über die Möglichkeit hochfrequente mechanische Schwingungen als diagnostisches Hilfsmittel zu verwerten. *Z. Neurol. Psychiat.*, 174(183), 1942.
14. J.H. Holmes, D.H. Howry, G.J. Posakony, and C.R. Cushman. The ultrasonic visualization of soft tissue structures in the human body. *Transactions of the American Clinical and Climatological Association*, 66(C):208–25, 1955.
15. D.H. Howry and W.R. Bliss. Ultrasonic visualization of soft tissue structures of the body. *J. Lab. Clin. Med.*, 40:579–592, 1952.
16. S.J. Norton and M. Linzer. Ultrasonic reflectivity imaging in three dimensions: Reconstruction with spherical transducer arrays. *Ultrasonic Imaging*, 1:210–31, 1979.
17. S.J. Norton and M. Linzer. Ultrasonic reflectivity imaging in three dimensions: Exact inverse scattering solutions for plane, cylindrical, and spherical apertures. *Biomedical Engineering, IEEE Transactions on*, BME-28(2):202–20, 1981.
18. S.J. Norton and M. Linzer. Ultrasonic reflectivity tomography: Reconstruction with circular transducer arrays. *Ultrasonic Imaging*, 1(2):154–84, 1979.
19. P.L. Carson, T.V. Oughton, W.R. Hendee, and S. Ahuja. Imaging soft tissue through bone with ultrasound transmission tomography by reconstruction. *Medical Pphysics*, 4(4):302–9, 1977.
20. G.H. Glover. Characterization of in vivo breast tissue by ultrasonic time of flight computed tomography. In *Proc. Nat. Bureau Standards 2nd Int. Symp. Ultrasonic Tissue Characterization*, page 221, 1977.
21. J.F. Greenleaf, S.A. Johnson, S.L. Lee, G.T. Herman, and E.H. Wood. Algebraic reconstruction of spatial distributions of acoustic absorption within tissue from their two-dimensional acoustic projections. In *Acoustic Holography*, volume 5, pages 591–603. Springer, 1974.
22. J.R. Klepper, G.H. Brandenburger, L.J. Busse, and J.G. Miller. Phase cancellation, reflection, and refraction effects in quantitative ultrasonic attenuation tomography. In *1977 Ultrasonics Symposium*, pages 182–8, 1977.

23. M. O'Donnell, J.W. Mimbs, B.E. Sobel, and J.B. Miller. Ultrasonic attenuation in normal and ischemic myocardium. In *Proc. Nat. Bureau Standards 2nd Int. Symp. Ultrasonic Tissue Characterization*, page 63, 1977.
24. J.F. Greenleaf, J. Ylitalo, and J.J. Gisvold. Ultrasonic computed tomography for breast examination. *IEEE Engineering in Medicine and Biology Magazine: The Quarterly Magazine of the Engineering in Medicine & Biology Society*, 6(4):27–32, 1987.
25. R.K. Mueller, M. Kaveh, and G. Wade. Reconstructive tomography and applications to ultrasonics. *Proceedings of the IEEE*, 67(4):567–87, 1979.
26. P.L. Carson, C.R. Meyer, A.L. Scherzinger, and T.V. Oughton. Breast imaging in coronal planes with simultaneous pulse echo and transmission ultrasound. *Science (New York, N.Y.)*, 214(4525):1141–3, 1981.
27. M. André, J. Wiskin, D. Borup, S. Johnson, H. Ojeda-Fournier, and L. Olson. Quantitative volumetric breast imaging with 3D inverse scatter computed tomography. In *Proceedings of the Annual International Conference of the IEEE Engineering in Medicine and Biology Society, EMBS*, pages 1110–3, 2012.
28. N. Duric, P. Littrup, S. Schmidt, C. Li, O. Roy, L. Bey-Knight, R. Janer, D. Kunz, X. Chen, J. Goll, A. Wallen, F. Zafar, V. Allada, E. West, I. Jovanovic, K. Li, and W. Greenway. Breast imaging with the SoftVue imaging system: First results. In *SPIE Proceedings Vol. 8675: Medical Imaging 2013: Ultrasonic Imaging, Tomography, and Therapy*, volume 8675, page 86750K, 2013.
29. E. Kretzek, M. Zapf, M. Birk, H. Gemmeke, and N.V. Ruiter. GPU based acceleration of 3D USCT image reconstruction with efficient integration into MATLAB. In Johan G. Bosch and Marvin M. Doyley, editors, *Proc. SPIE 8675, Medical Imaging 2013: Ultrasonic Imaging, Tomography, and Therapy*, page 86750O, 2013.
30. P. Pellegretti, M. Vicari, M. Zani, M. Weigel, D. Borup, J. Wiskin, U. Saueressig, E. Kotter, and M. Langer. A clinical experience of a prototype automated breast ultrasound system combining transmission and reflection 3D imaging. In *IEEE International Ultrasonics Symposium, IUS*, pages 1407–10, 2011.
31. O. Roy, S. Schmidt, C. Li, V. Allada, E. West, D. Kunz, and N. Duric. Breast imaging using ultrasound tomography: From clinical requirements to system design. *2013 IEEE International Ultrasonics Symposium (IUS)*, pages 1174–7, 2013.
32. B. Malik, E. Iuanow, and J. Klock. An exploratory multi-reader, multi-case study comparing transmission ultrasound to mammography on recall rates and detection rates for breast cancer lesions. *Academic Radiology*, 2020.
33. N. Duric, P. Littrup, P. Chandiwala-Mody, C. Li, S. Schmidt, L. Myc, O. Rama, L. Bey-Knight, J. Lupinacci, B. Ranger, A. Szczepanski, and E. West. In-vivo imaging results with ultrasound tomography: Report on an ongoing study at the Karmanos Cancer Institute. In *SPIE Proceedings Vol. 7629: Medical Imaging 2010: Ultrasonic Imaging, Tomography, and Therapy*, page 76290M, 2010.
34. G. Zografos, P. Liakou, D. Koulocheri, I. Liovarou, M. Sofras, S. Hadjiagapis, M. Orme, and V. Marmarelis. Differentiation of BIRADS-4 small breast lesions via multimodal Ultrasound Tomography. *European radiology*, 25(2):410–8, 2015.
35. N.V. Ruiter, M. Zapf, R. Dapp, T. Hopp, W.A. Kaiser, and H. Gemmeke. First results of a clinical study with 3D Ultrasound Computer Tomography. *2013 IEEE International Ultrasonics Symposium (IUS)*, pages 651–4, 2013.
36. F. Natterer. *The mathematics of computerized tomography*. Society for Industrial and Applied Mathematics, 2001.
37. R. Dapp. *Abbildungsmethoden für die Brust mit einem 3D-Ultraschall-Computertomographen*. Dissertation, Karlsruher Institut f"ur Technologie, 2013.
38. J. Wiskin, D.T. Borup, S.A. Johnson, and M. Berggren. Non-linear inverse scattering: High resolution quantitative breast tissue tomography. *The Journal of the Acoustical Society of America*, 131(5):3802–13, 2012.
39. G.Y. Sandhu, C. Li, O. Roy, S. Schmidt, and N. Duric. Frequency domain ultrasound waveform tomography: Breast imaging using a ring transducer. *Physics in Medicine and Biology*, 60(14):5381–98, 2015.

40. S.R. Doctor, T.E. Hall, and L.D. Reid. SAFT - the evolution of a signal processing technology for ultrasonic testing, 1986.
41. G.F. Schwarzenberg, H. Gemmeke, and N.V. Ruiter. 3D PSF analysis for arbitrary transducer geometries and SAFT-based image reconstruction. In Stephen A. McAleavey and Jan D'hooge, editors, *SPIE Proceedings Vol. 6920: Medical Imaging 2008: Ultrasonic Imaging and Signal Processing*, page 69200A, 2008.
42. J. Rouyer, S. Mensah, E. Franceschini, P. Lasaygues, and J.-P. Lefebvre. Conformal ultrasound imaging system for anatomical breast inspection. *IEEE Transactions on Ultrasonics, Ferroelectrics, and Frequency Control*, 59(7):1457–69, 2012.
43. B. Malik, R. Terry, J. Wiskin, and M. Lenox. Quantitative transmission ultrasound tomography: Imaging and performance characteristics. *Medical Physics*, 45(7):3063–3075, 2018.
44. V.Z. Marmarelis, J. Jeong, D.C. Shin, and S. Do. High-resolution 3-D imaging and tissue differentiation with transmission tomography. In M.P. André et al., editor, *Acoustical Imaging*, volume 28 of *Acoustical Imaging*, pages 195–206. Springer Netherlands, 2007.
45. K. Tae-Seong. 3-D high resolution Ultrasonic Transmission Tomography and soft tissue differentiation. *Journal of Biomedical Engineering Research*, 26(1):55–63, 2005.
46. A. Suzuki, Y. Tsubota, T. Terada, H. Yamashita, F. Kato, M. Nishida, M. Satoh, and K. Kawabata. Optimized source estimation for full waveform inversion in ultrasound computed tomography. In Brett C. Byram and Nicole V. Ruiter, editors, *Medical Imaging 2021: Ultrasonic Imaging and Tomography*, volume 11602, pages 32 – 39. International Society for Optics and Photonics, SPIE, 2021.
47. M. Ding, J. Song, L. Zhou, S. Wang, and M. Yuchi. In vitro and in vivo evaluations of breast ultrasound tomography imaging system in HUST. In Neb Duric and Brett C. Byram, editors, *Medical Imaging 2018: Ultrasonic Imaging and Tomography*, volume 10580, pages 162 – 169. International Society for Optics and Photonics, SPIE, 2018.
48. N.V. Ruiter, G. Göbel, L. Berger, M. Zapf, and H. Gemmeke. Realization of an optimized 3D USCT. In Jan D'hooge and Marvin M. Doyley, editors, *Proc. SPIE. 7968, Medical Imaging 2011: Ultrasonic Imaging, Tomography, and Therapy*, page 796805, 2011.
49. S. Webb. *The physics of medical imaging*. Hilger, Bristol Philadelphia, 1988.
50. M. Linzer and S.J. Norton. Ultrasonic tissue characterization. *Annual review of biophysics and bioengineering*, 11(4):303–29, 1982.
51. J.F. Greenleaf. A graphical description of scattering. *Ultrasound in Medicine & Biology*, 12(8):603–9, 1986.
52. C.M. Sehgal and J.F. Greenleaf. Scattering of ultrasound by tissues. *Ultrasonic Imaging*, 6(1):60–80, 1984.
53. A. Günter. *Quantitative Analyse und objektive Darstellung von Ultraschallbildern zur medizinischen Diagnose*. Dissertation, Universität Karlsruhe, 2002.
54. U. Taskin. *Full-Waveform Inversion for Breast Ultrasound*. PhD thesis, Delft University of Technology, 2021.
55. J. Virieux and S. Operto. An overview of full-waveform inversion in exploration geophysics. *Geophysics*, 74(6):WCC1–26, 2009.
56. F. Natterer. Acoustic mammography in the time domain. Technical report, University Muenster, 2008.
57. N. Özmen, R. Dapp, M. Zapf, H. Gemmeke, N.V. Ruiter, and K.W.A. van Dongen. Comparing different ultrasound imaging methods for breast cancer detection. *IEEE Transactions on Ultrasonics, Ferroelectrics, and Frequency Control*, 62(4):637–46, 2015.
58. X. Zhang, S.L. Broschat, and P.J. Flynn. A numerical study of conjugate gradient directions for an ultrasound inverse problem. *Journal of Computational Acoustics*, 12(4):587–604, 2004.
59. A.V. Goncharsky and S.Y. Romanov. Supercomputer technologies in inverse problems of ultrasound tomography. *Inverse Problems*, 29:075004, 2013.
60. M.C. Hesse, L. Salehi, and G. Schmitz. Nonlinear simultaneous reconstruction of inhomogeneous compressibility and mass density distributions in unidirectional pulse-echo ultrasound imaging. *Physics in Medicine and Biology*, 58(17):6163–78, 2013.

61. K.W.A. van Dongen and W.M.D. Wright. A full vectorial contrast source inversion scheme for three-dimensional acoustic imaging of both compressibility and density profiles. *The Journal of the Acoustical Society of America*, 121:1538–49, 2007.
62. J.B Keller. Accuracy and validity of the Born and Rytov approximations. *Journal of the Optical Society of America*, 59(8):1003–4, 1969.
63. M.P. André, H.S. Janee, P.J. Martin, G.P. Otto, B.A. Spivey, and D.A. Palmer. High-speed data acquisition in a diffraction tomography system employing large-scale toroidal arrays. *International Journal of Imaging Systems and Technology*, 8(1):137–47, 1997.
64. T.L. Chenevert, D.I. Bylski, P.L. Carson, C.R. Meyer, P.H. Bland, D.D. Adler, and R.M. Schmitt. Ultrasonic computed tomography of the breast. Improvement of image quality by use of cross-correlation time-of-flight and phase-insensitive attenuation measurements. *Radiology*, 152(1):155–9, 1984.
65. F. Simonetti, L. Huang, and N. Duric. A multiscale approach to diffraction tomography of complex three-dimensional objects. *Applied Physics Letters*, 95, 2009.
66. M. Hardt. *Distributed Simulations for 3D Ultrasound Computer Tomography. Acoustic wave simulations for a new breast cancer imaging device*. Ph.d. thesis, University of Karlsruhe, 2012.
67. R.J. Lavarello and M.L. Oelze. Tomographic reconstruction of three-dimensional volumes using the distorted Born iterative method. *IEEE Transactions on Medical Imaging*, 28(10):1643–53, 2009.
68. S.-H. Hung, F. A. Dahlen, and G. Nolet. Frechet kernels for finite-frequency traveltimes-II. Examples. *Geophysical Journal International*, 141:175–203, 2000.
69. L. Althaus. *On acoustic tomography using paraxial approximations*. Master thesis, Universität Darmstadt, 2015.
70. H. Wang, X. Qian, H. Gemmeke, T. Hopp, N. V. Ruiter, and J. Hesser. Fast image reconstruction in ultrasound transmission tomography by U-net. In *2020 Virtual IEEE Nuclear Science Symposium and Medical Imaging Conference*, 2020.
71. A.H. Andersen. A ray tracing approach to restoration and resolution enhancement in experimental ultrasound tomography. *Ultrasonic Imaging*, 12(4):268–91, 1990.
72. C. Li, N. Duric, P. Littrup, and L. Huang. In vivo breast sound-speed imaging with Ultrasound Tomography. *Ultrasound in Medicine and Biology*, 35(10):1615–28, 2009.
73. R. Dapp, H. Gemmeke, and N.V. Ruiter. 3D refraction-corrected transmission reconstruction for 3D Ultrasound Computer Tomography. In Johan G. Bosch and Marvin M. Doyley, editors, *SPIE Medical Imaging 2012: Ultrasonic Imaging, Tomography, and Therapy*, pages 832014–832014–7, 2012.
74. C. Li, N. Duric, and L. Huang. Breast imaging using transmission ultrasound: Reconstructing tissue parameters of sound speed and attenuation. *BioMedical Engineering and Informatics: New Development and the Future - Proceedings of the 1st International Conference on BioMedical Engineering and Informatics, BMEI 2008*, 2:708–12, 2008.
75. J. Spetzler and R. Snieder. The Fresnel volume and transmitted waves. *Geophysics*, 69(3):653–63, 2004.
76. P.R. Williamson. A guide to the limits of resolution imposed by scattering in ray tomography. *Geophysics*, 56(2):202–7, 1991.
77. R. Dapp, M. Zapf, and N.V. Ruiter. Geometry-independent speed of sound reconstruction for 3D USCT using apriori information. In *2011 IEEE International Ultrasonics Symposium*, pages 1403–6, October 2011.
78. E. Kretzek and N.V. Ruiter. GPU based 3D SAFT reconstruction including phase aberration. In Johan G. Bosch and Marvin M. Doyley, editors, *Proc. SPIE 9040, Medical Imaging 2014: Ultrasonic Imaging and Tomography*, page 90400W, 2014.
79. Thomas H. Cormen, Charles E. Leiserson, Ronald L. Rivest, and Clifford Stein. *Introduction to Algorithms*. MIT Press, Cambridge, 1990.
80. USCT Exchange and Collaboration Platform. http://ipeusctdb1.ipe.kit.edu/ usct/challenge/. Accessed: 2021-04-21.

81. N.V. Ruiter, M. Zapf, T. Hopp, H. Gemmeke, K.W.A. van Dongen, J. Camacho, C. Fritsch, J.F. Cruza, J.L. Herraiz, M. Perez Liva, and J.M. Udias. The usct reference database. In *Proceedings of the International Workshop on Medical Ultrasound Tomography: 1.- 3. Nov. 2017, Speyer, Germany. Hrsg.: T. Hopp*, pages 385–394. KIT Scientific Publishing, 2018. 54.02.02; LK 01.
82. R. Stotzka, H. Widmann, T.O. Müller, K. Schlote-Holubek, H. Gemmeke, N.V. Ruiter, and G. Göbel. Prototype of a new 3D Ultrasound Computer Tomography system: Transducer design and data recording. In William F. Walker and Stanislav Y. Emelianov, editors, *Proc. SPIE. 5373, Medical Imaging 2004: Ultrasonic Imaging and Signal Processing*, pages 70–9, 2004.
83. Jorge Camacho, Luis Medina, Jorge Cruza, Jose Moreno, and Carlos Fritsch. Multimodal ultrasonic imaging for breast cancer detection. *Archives of Acoustics*, 37(3), 2013.
84. L. Medina-Valdés, M. Pérez-Liva, J. Camacho, J.M. Udías, J.L. Herraiz, and N. González-Salido. Multi-modal ultrasound imaging for breast cancer detection. *Physics Procedia*, 63:134–140, 2015. 43rd Annual UIA Symposium 23—25 April 2014 CSIC Madrid, Spain.
85. Ting Chen, Junseob Shin, and Lianjie Huang. Ultrasound transmission attenuation tomography using energy-scaled amplitude ratios. In Neb Duric and Brecht Heyde, editors, *Medical Imaging 2016: Ultrasonic Imaging and Tomography*, volume 9790, pages 324 – 330. International Society for Optics and Photonics, SPIE, 2016.
86. J. Wiskin, D. Borup, and S. Johnson. Inverse scattering theory. In M.P. André, J.P. Jones, and H. Lee, editors, *Acoustical Imaging*, volume 30, pages 53–9. Springer Netherlands, 2011.
87. H. Gemmeke, L. Berger, T. Hopp, M. Zapf, W. Tan, R. Blanco, R. Leys, I. Peric, and N.V. Ruiter. The new generation of the kit 3d usct. In *Proceedings of the International Workshop on Medical Ultrasound Tomography: 1.- 3. Nov. 2017, Speyer, Germany. Hrsg.: T. Hopp*, pages 271–282. KIT Scientific Publishing, 2018. 54.02.02; LK 01.
88. J. Wiskin, D. Borup, S. Johnson, M. André, J. Greenleaf, Y. Parisky, and J. Klock. Three-dimensional nonlinear inverse scattering: Quantitative transmission algorithms, refraction corrected reflection, scanner design and clinical results. In *Proceedings of Meetings on Acoustics*, volume 19, 2013.
89. T. Misaridis and J.A. Jensen. Use of modulated excitation signals in medical ultrasound. Part I: Basic concepts and expected benefits. *IEEE transactions on ultrasonics, ferroelectrics, and frequency control*, 52(2):177–91, 2005.
90. W.Y. Tan, T. Steiner, and N.V. Ruiter. Newton's method based self calibration for a 3D Ultrasound Tomography System. In *2015 IEEE International Ultrasonics Symposium (IUS)*, pages 1–4, 2015.
91. C. Cueto, L. Guasch, J. Cudeiro, O. Calderon Agudo, O. Bates, G. Strong, and M.-X. Tang. Spatial response identification enables robust experimental ultrasound computed tomography, 2021.
92. T. Fischer, U. Bick, and A. Thomas. Mammographie-Screening in Deutschland. *Visions Journal*, 2007.
93. J.F. Greenleaf. Quantitative cross-sectional imaging of ultrasound parameters. *Ultrasonics Symposium Proceedings*, pages 989–95, 1977.
94. F.T. D'Astous and F.S. Foster. Frequency dependence of ultrasound attenuation and backscatter in breast tissue. *Ultrasound in Medicine & Biology*, 12(10):795–808, 1986.
95. P.D. Edmonds, C.L. Mortensen, J.R. Hill, S.K. Holland, J.F. Jensen, P. Schattner, and A.D. Valdes. Ultrasound tissue characterization of breast biopsy specimens. *Ultrasonic Imaging*, 13(2):162–85, 1991.
96. C.L. Mortensen, P.D. Edmonds, Y. Gorfu, J.R. Hill, J.F. Jensen, P. Schattner, L.A. Shifrin, A.D. Valdes, S.S. Jeffrey, and L.J. Esserman. Ultrasound tissue characterization of breast biopsy specimens: Expanded study. *Ultrasonic imaging*, 18(3):215–30, 1996.
97. M.P. André, C.H. Barker, N. Sekhon, J. Wiskin, D. Borup, and K. Callahan. Pre-clinical experience with full-wave inverse-scattering for breast imaging. In Iwaki Akiyama, editor, *Acoustical Imaging*, volume 29 of *Acoustical Imaging*, pages 73–80. Springer Netherlands, 2009.

98. T. Hopp, N. Duric, and N.V. Ruiter. Image fusion of Ultrasound Computer Tomography volumes with X-ray mammograms using a biomechanical model based 2D/3D registration. *Computerized Medical Imaging and Graphics*, 40:170–81, 2015.
99. N. Duric, P. Littrup, C. Li, O. Rama, L. Bey-Knight, S. Schmidt, and J. Lupinacci. Detection and characterization of breast masses with ultrasound tomography: Clinical results. In Stephen A. McAleavey and Jan D'hooge, editors, *SPIE Proceedings Vol. 7265: Medical Imaging 2009: Ultrasonic Imaging and Signal Processing*, volume 7265, page 72651G, 2009.
100. N. Duric, P. Littrup, M. Sak, C. Li, D. Chen, O. Roy, L. Bey-Knight, and R. Brem. A Novel Marker, Based on Ultrasound Tomography, for Monitoring Early Response to Neoadjuvant Chemotherapy. *Journal of Breast Imaging*, 2(6):569–576, 10 2020.
101. M. Sak, N. Duric, R. Pfeiffer, M. Sherman, P. Littrup, M. Simon, D. Gorski, T. Albrecht, H. Ali, R. Brem, S. Fan, and G. Gierach. Abstract p3-08-28: Tissue sound speed is more strongly associated with breast cancer risk than mammographic percent density: A comparative case-control study. *Cancer Research*, 80(4 Supplement):P3–08–28–P3–08–28, 2020.
102. M. Yamashita. Delphinus softvue prospective case collection - arm 1 (sv pcc arm1). https://www.clinicaltrials.gov/ct2/show/record/NCT03257839. Accessed: 2021-11-08.
103. B. Malik, S. Lee, R. Natesan, and J. Wiskin. Clustering based quantitative breast density assessment using 3D transmission ultrasound. In Brett C. Byram and Nicole V. Ruiter, editors, *Medical Imaging 2020: Ultrasonic Imaging and Tomography*, volume 11319, pages 91 – 96. International Society for Optics and Photonics, SPIE, 2020.
104. Case collection study to determine the accuracy, call back and cancer detection rates of qt ultrasound in breast imaging (accrue). https://www.clinicaltrials.gov/ct2/show/NCT03052166. Accessed: 2021-11-08.
105. P. Lasaygues, J. Rouyer, S. Mensah, E. Franceschini, G. Rabau, R. Guillermin, S. Bernard, V. Monteiller, and D. Komatitsch. Non-linear ultrasonic computed tomography (usct) for soft and hard tissue imaging. In *Proceedings of the Int. Workshop on Medical Ultrasound Tomography*.
106. J. Wiskin, B. Malik, R. Natesan, N. Pirshafiey, J. Klock, and M. Lenox. 3D full inverse scattering ultrasound tomography of the human knee (Conference Presentation). In Brett C. Byram and Nicole V. Ruiter, editors, *Medical Imaging 2019: Ultrasonic Imaging and Tomography*, volume 10955. International Society for Optics and Photonics, SPIE, 2019.
107. J. Wiskin, B. Malik, V. Theendakara, and J. Klock. Orthopedic and myopathic imaging with transmission ultrasound tomography: experimental verification, quantitative accuracy and clinical implications. In Brett C. Byram and Nicole V. Ruiter, editors, *Medical Imaging 2020: Ultrasonic Imaging and Tomography*, volume 11319, pages 175 – 182. International Society for Optics and Photonics, SPIE, 2020.
108. J. Wiskin, B. Malik, N. Pirshafiey, and J. Klock. Limited view reconstructions with transmission ultrasound tomography: clinical implications and quantitative accuracy. In Brett C. Byram and Nicole V. Ruiter, editors, *Medical Imaging 2020: Ultrasonic Imaging and Tomography*, volume 11319, pages 167 – 174. International Society for Optics and Photonics, SPIE, 2020.
109. L. Guasch, O. Calderón Agudo, M.-X. Tang, P. Nachev, and M. Warner. Full-waveform inversion imaging of the human brain. *npj Digital Medicine*, 3(1):28, 2020.
110. T. J. Dubinsky, C. Cuevas, M. K. Dighe, O. Kolokythas, and J. H. Hwang. High-intensity focused ultrasound: Current potential and oncologic applications. *AJR American journal of roentgenology*, 190(1):191–199, 2008.
111. T. Yu, X. Fan, S. Xiong, K. Hu, and Z. Wang. Microbubbles assist goat liver ablation by high intensity focused ultrasound. *Eur Radiol.*, 16(7):1557–63, 2006.
112. Z.W. Qian, L. Xiong, J. Yu, D. Shao, H. Zhu, and X. Wu. Noninvasive thermometer for hifu and its scaling. *Ultrasonics*, 44:e31–e35, 2006. Proceedings of Ultrasonics International (UI'05) and World Congress on Ultrasonics (WCU).
113. X. Fan and K. Hynynen. Ultrasound surgery using multiple sonications–treatment time considerations. *Ultrasound Med Biol.*, 22(4), 1996.

114. J. Jensen, S.I. Nikolov, Alfred Yu, and Damien Garcia. Ultrasound vector flow imaging: Ii: Parallel systems. *IEEE Transactions on Ultrasonics, Ferroelectrics, and Frequency Control*, 63:1–1, 11 2016.
115. Nuria Salido, Lidia Medina, and Jorge Camacho. Full angle spatial compound of arfi images for breast cancer detection. *Ultrasonics*, 71, 06 2016.
116. T. Hopp and N. V. Ruiter. Strain elastography with ultrasound computer tomography: a simulation study based on biomechanical models. In Brett C. Byram and Nicole V. Ruiter, editors, *Medical Imaging 2021: Ultrasonic Imaging and Tomography*, volume 11602, pages 194 – 201. International Society for Optics and Photonics, SPIE, 2021.
117. Q. Chen, H. Song, J. Yu, and K. Kim. Current development and applications of super-resolution ultrasound imaging. *Sensors (Basel, Switzerland)*, 21(7):2417, 04 2021.
118. M. Tanter and M. Fink. Ultrafast imaging in biomedical ultrasound. *IEEE transactions on ultrasonics, ferroelectrics, and frequency control*, 61:102–119, 01 2014.
119. C. Errico, J. Pierre, S. Pezet, Y. Desailly, Z. Lenkei, O. Couture, and M. Tanter. Ultrafast ultrasound localization microscopy for deep super-resolution vascular imaging. *Nature*, 527(7579):499–502, 2015.
120. S. Manohar and M. Dantuma. Current and future trends in photoacoustic breast imaging. *Photoacoustics*, 16:100134, 2019.
121. E. Kretzek, P. Hucker, M. Zapf, and N.V. Ruiter. Evaluation of directional reflectivity characteristics as new modality for 3D Ultrasound Computer Tomography. In *2015 IEEE International Ultrasonics Symposium (IUS)*, 2015.
122. S. Nikolov and J.A. Jensen. Virtual ultrasound sources in high-resolution ultrasound imaging. In Michael F. Insana and William F. Walker, editors, *Medical Imaging 2002: Ultrasonic Imaging and Signal Processing*, volume 4687, pages 395 – 405. International Society for Optics and Photonics, SPIE, 2002.
123. T. Misaridis and P. Munk. High frame rate imaging using parallel transmission of focused coded fields [medical ultrasound imaging applications]. In *IEEE Ultrasonics Symposium 2004*, volume 2, pages 1417–20, 2004.